



UNIVERSITY OF
CAMBRIDGE

Department of Engineering

Propulsion Systems for VTOL Electric Vehicles

Author Name: JORDAN SANDBERG ERIKSEN

Supervisor: Dr. SAMUEL GRIMSHAW

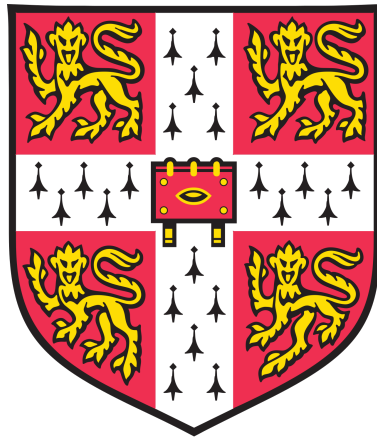
Date: 27th May 2020

I hereby declare that, except where specifically indicated, the work submitted herin is my own original work.

Signed _____ date _____ 27th May 2020

UNIVERSITY OF CAMBRIDGE
DEPARTMENT OF ENGINEERING

MASTERS PROJECT REPORT



Propulsion Systems for VTOL Electric Vehicles

Jordan Sandberg Eriksen

SUPERVISED BY: Dr Sam Grimshaw

Abstract

The design problem of selecting the best propulsor for an electric vertical take off and landing (e-VTOL) application is explored, and a novel criterion is proposed for directly comparing performance of an electric ducted fan (EDF) and propeller in hover. A turbomachinery design approach is used to develop a ducted fan with a non-dimensional thrust to power ratio 103% higher than a VTOL optimised propeller. It is shown that payload size and relative EDF flow area, with respect to propeller area, determines which propulsion system is most suitable. A modular flying test bed with a quadcopter configuration is developed to test each propulsion system.

The report opens with a discussion on current trends in e-VTOL design, noting the range of both propeller and EDF driven systems being developed. The relative merits of an EDF compared to a propeller are explored, concluding that without further analysis there is no clear choice between the two. Literature on the use of EDFs in unmanned aerial vehicles (UAVs) and personal aerial vehicles (PAVs) focuses on fan and duct geometry as well as ducted fan performance in various operating conditions, but does not address the systems level approach needed to design for a general application. The absence of a turbomachinery approach to fan design is also noted. Both a turbomachinery and systems level approach are taken in the report.

The non-dimensional thrust to power ratio, known as figure of merit, is presented as a method of quantifying propulsor performance in hover and its failure to account for propulsor weight is noted, showing an ideal ducted fan with a straight exit duct has a theoretical figure of merit 41% larger than an ideal propeller, as in Pereira^[1]. A novel ‘superiority parameter’ is presented from which the most suitable propulsor for a given application can be determined. Requiring less power to maintain static hover with a given payload is achieved when a propulsor’s superiority parameter is positive. The design of a 1kg modular flying test bed system is presented. This enables the comparison of a ducted fan and propeller to be made using the superiority parameter.

The aerodynamic design of a 3D printed EDF, required to propel the flying test bed in hover, is presented. The superiority parameter across a geometric design space is evaluated, using a mass model to estimate propulsor weight. The EDF has a single low Reynolds number rotor-stator stage and a diffusing exit duct that gives a theoretical figure of merit 51% higher than an ideal propeller. Mechanical and electrical design is considered and an embodied propulsor design presented.

Propulsors are tested on a fixed test stand to determine stationary performance. The propeller is found to have an aerodynamic efficiency of 67%. The EDF figure of merit is 103% larger than the propeller, with an aerodynamic efficiency of 90%.

Aerodynamic loss is hypothesised to result primarily from low Reynolds number flow separation from the blades, skin friction from high surface roughness, and shroud clearance flow loss. The superiority parameter was found to be within 2% of the predicted value, validating the mass model. At the design payload the superiority condition is not satisfied, however, the range of payloads and propulsor area ratios required to satisfy the superiority condition are evaluated and a design chart is presented, enabling the choice of EDF or propeller for a given application to be made.

Recommendations for future work are rationalised in light of the project outcomes. In particular, contra-rotating EDFs (CRDFs) are discussed as having the most potential for further study. As in Waldren *et al.*^[2], thrust output can double compared to a non-contra-rotating ducted fan (NDF) meaning fewer propulsors are required to maintain hover. The superiority condition can be satisfied at lower payloads and propulsor area ratios when using a CRDF compared to a NDF, due to the subsequent reduction in propulsor weight.

Contents

1	Introduction	1
1.1	Literature Review	2
1.2	Comparison of Ducted Fan and Propeller Performance	4
1.3	Research Question	6
2	Flying Test Bed System Design	7
2.1	Flying Test Bed	7
3	Ducted Fan Aerodynamic Design	10
3.1	Introduction	10
3.2	Mean-line Design	10
3.3	3D Blade Design	17
4	Electrical and Mechanical Design	24
4.1	Introduction	24
4.2	Electrical Design	24
4.3	Mechanical Design	25
5	Test Facility Design	29
5.1	Cage Design & Tether	29
5.2	System Calibration	29
5.3	Stationary Propulsor Test	30
5.4	Hover Test	32
5.5	Measurement Techniques	33
6	Results	36
6.1	Stationary Propulsor Test	36
6.2	Performance Comparison and Discussion	37
6.3	Superiority Condition	42
6.4	Hover Tests	43
7	Future Work	44
7.1	Propulsor Design	44
7.2	Stationary Propulsor Experiments	45
7.3	Flying Test Bed Experiments	46
8	Conclusions	47

Nomenclature

Flow Properties

h_0	Stagnation enthalpy	$kJ \cdot kg^{-1}$	s	Entropy $kJ \cdot kg^{-1} \cdot K^{-1}$
m_l	Leakage mass flow rate	$kg \cdot s^{-1}$	V	Velocity $m \cdot s^{-1}$
m_m	Mainstream mass flow rate	$kg \cdot s^{-1}$	α	Absolute flow angle $(^\circ)$
m_δ	Carter deviation constant		β	Relative flow angle $(^\circ)$
\dot{m}	Mass flow rate	$kg \cdot s^{-1}$	γ	CRDF rotor 2 relative flow angle $(^\circ)$
p	Static pressure	Pa	δ	Deviation $(^\circ)$
p_0	Stagnation pressure	Pa	ρ	Density $kg \cdot m^{-3}$
			θ	Flow turning $(^\circ)$
			Θ	Temperature K

Geometry

A	Area	m^2	g_t	Shroud clearance	m
c	Chord	m	HTR	Hub to tip ratio	
l	Span	m	L	Length	m
r	Radius	m	σ	Exit duct area ratio	
s	Pitch	m			

Electro-mechanical Properties

E	Electro-motive force (EMF)	V	R	Resistance	<i>Ohms</i>
I_{ZZ}	Moment of inertia about rotation axis	$kg \cdot m^2$	T	Thrust	N
k_t	Torque constant	$V \cdot s \cdot rad^{-1}$	U	Blade speed	$m \cdot s^{-1}$
k_v	Voltage constant	$rads^{-1} \cdot V^{-1}$	W	Weight	N
m	Mass	kg	Ω	Rotor angular velocity	$rad \cdot s^{-1}$
N_P	Number of propulsors		$\dot{\Omega}$	Rotor angular acceleration	$rad \cdot s^{-2}$
P	Power	W	τ_e	Motor torque	$N \cdot m$
			τ_s	Shaft torque	$N \cdot m$

Non-dimensional Quantities

C_{pr}	Static pressure recovery coefficient	Λ	Propulsor area ratio
M_F	Figure of merit	Σ	Superiority parameter
Re	Reynolds number	ϕ	Flow coefficient
η_a	Aerodynamic efficiency	ψ	Stage loading
$\eta_{sys.}$	System efficiency		

Subscripts

$()_0$	Control volume inlet plane	$()_h$	Hub
$()_1$	Rotor inlet plane	$()_in$	Propulsor inlet plane
$()_2$	Rotor exit plane	$()_m$	Mean-line
$()_3$	Stator exit plane	$()_max$	Maximum value
$()_{atm.}$	Atmospheric	$()_{prop.}$	Propeller
$()_c$	Casing	$()_s$	Shaft
$()_e$	Propulsor exit	$()_x$	Blade passage axial
$()_{fan}$	Fan		

Abbreviations

BLDCM	Brush-less DC motor	PAV	Personal aerial vehicle
CFRP	Carbon fibre reinforced plastic	PLA	Poly-lactic acid
CRDF	Contra-rotating ducted fan	RHS	Right hand side
DC	Direct current	RMS	Root mean squared
EDF	Electric ducted fan	SFEE	Steady flow energy equation
eVTOL	[Electric] vertical take-off and landing	SFME	Steady flow momentum equation
FEA	Finite element analysis	UAV	Unmanned aerial vehicle
LHS	Left hand side	UROP	Undergraduate research opportunity
NDF	Non-contra-rotating ducted fan		



(a) Open propeller VTOL designs. **Left to right** Ehang 216 Autonomous Air Vehicle; Rolls-Royce VTOL; Wisk Cora eVTOL



(b) Ducted propeller/fan VTOL designs. **Left to right** Airbus Citybus; Bell NEXUS; Lilium Jet

Figure 1.1: Various propulsion systems used in recent eVTOL developments

1 Introduction

New aerospace markets are forecast to have a value of \$210-\$360 billion by 2040^[3]. These markets are accounted for by the unmanned goods transport (21%) and the passenger transport (79%) sectors, both strongly influencing the electric vertical take-off and landing (e-VTOL) market trebling between 2019 - 2024^[4]. VTOL personal and unmanned goods transport reduces travelling time and does not require significant transport infrastructure to operate. Electric propulsion systems have zero emissions and lower running costs, and have opened up the aerodynamic design space with over 200 electrically propelled vehicles currently in development^[5]. Many different design solutions are being explored, some of which are shown in Fig. 1.1. The main design difference between these is the choice of open propeller or ducted fan. By increasing the pressure downstream of the propulsor and creating a low pressure region above it, ducted fans benefit from increased thrust for the same input power. Ducted fans also benefit from improved safety as well as containment in an emergency situation. However, ducting also adds weight. If the ducted fan power requirement for a specific application can match or improve on that of an open propeller, these additional benefits make the ducted fan the preferred propulsion method. Therefore, the application affects the choice of propulsor.

This report presents a method by which a ducted fan and an open propeller can be compared. A condition is derived enabling comparison of the power requirement of a propulsor for a given application, and is applied to the design of a ducted fan that aims to require less power than a propeller when carrying a 1kg load. The condition is also used to explore the design space and suggest which applications could benefit from the use of ducted fans.

1.1 Literature Review

1.1.1 Previous Work and Motivation

Studies on ducted fans have been conducted since the 1930s, and there has been a recent rise in research in the field due to the increased interest in personal aerial vehicles (PAVs) and unmanned aerial vehicles (UAVs). Zhang *et al.*^[6] presents the state-of-the-art in ducted fan research, providing a full survey of around 90 published works. Research methods are divided into experimental, numerical modelling, computational fluid dynamics (CFD) and optimisation. The six design challenges proposed by Zhang are: crosswind effects, tip clearance flows, high-speed performance, noise emissions, control systems, and contra-rotating ducted fan systems.

Zhang shows experiments to test primarily ducted propellers (without stators), modelled using blade element theory and lifting line theory; as opposed to the turbomachinery approach based on turning and loss that is prevalent in turbo-jet and turbo-fan design. The relative merits of a turbomachinery approach, compared to conventional propeller theory, when designing ducted fans is unclear. A turbomachinery design approach is taken in this report.

Extensive work has been undertaken on inlet geometry design for both static hover and cross-wind conditions. Exit duct area ratio is recognised across all research methods as the primary factor affecting performance, however Zhang comments on the lack of an integrated approach to design and optimisation. Taking this approach to propulsion system design, for a specific application, is key to understanding how to improve on the performance of an open propeller; no work is noted to have done this, and so this report explores this design approach.

Contra-rotating systems are identified to be important for redundancy and torque balancing as well as having the potential to increase thrust density. Recent studies^[7] lack support from experiment or simulation, and performance determining design parameters need further investigation.

1.1.2 Analysis Methods

The performance of a propulsor in hover can be quantified by the figure of merit, M_F , defined as a non-dimensional thrust-to-power ratio. From Pereira^[1]

$$M_F = \frac{T}{P} \sqrt{\frac{T}{2\rho A_x}} \quad (1.1)$$

where A_x , the blade passage axial flow area, can be related to the exit duct exit area, A_e , by the area ratio

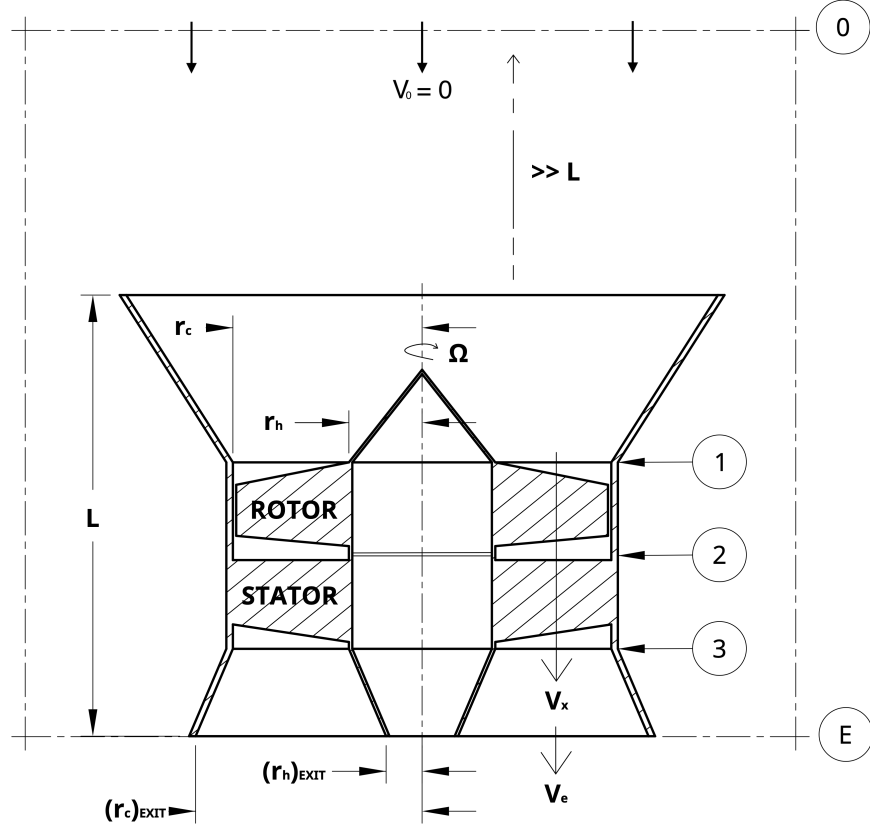


Figure 1.2: Cross-section of ducted fan configuration and control volume with geometric variables (radius r , length L) and fan speed Ω shown. **0** Control volume inlet plane; **1** Rotor inlet plane; **2** Inter-rotor-stator plane; **3** Stator exit plane; **E** Exit duct/control volume exit plane.

$$\sigma = \frac{A_e}{A_x} \quad (1.2)$$

Considering the control volume around the ducted fan in Fig. 1.2, the thrust generated by the fan can be determined from the steady flow momentum equation (SFME). Assuming zero inlet swirl and straight and parallel exit flow (zero exit swirl), the static pressure at exit, p_e , is equal to atmospheric pressure, p_{atm} . Considering continuity

$$\dot{m} = \rho A_x V_x = \rho A_e V_e \quad \therefore \sigma = \frac{V_x}{V_e} \quad (1.3)$$

The SFME can be written in terms of the blade passage axial quantities (A_x and V_x) and the area ratio, σ

$$T = \dot{m} V_e \quad \therefore T = \frac{\rho A_x V_x^2}{\sigma} \quad (1.4)$$

Flow power is determined from the steady flow energy equation (SFEE)

$$P = \frac{1}{2}\dot{m}V_e^2 \quad \therefore P = \frac{\rho A_x V_x^3}{2\sigma^2} \quad (1.5)$$

Substituting Eqn. 1.4 and Eqn. 1.5 into Eqn. 1.1 gives a simplified expression for figure of merit of a ducted fan:

$$M_F = \sqrt{2\sigma} \quad (1.6)$$

Pereira^[1] shows the maximum figure of merit for a propeller to be 1. Provided the area ratio of the exit duct on a ducted fan remains $\sigma > 0.5$, ducted fan figure of merit is greater.

1.2 Comparison of Ducted Fan and Propeller Performance

Figure of merit characterises propulsor performance in static hover, however, it does not consider the extra propulsor weight associated with a ducted fan (due to casing, intake, and diffuser) and the resulting increase in required thrust. The power required for a ducted fan to maintain static hover must be less than that required from a propeller.

To maintain static hover, the propulsor thrust, T , must satisfy $W = T \cdot N_P$, where N_P is the number of propulsors and W is the vehicle weight for a given application. The shaft power required by a propeller is evaluated by considering figure of merit (expressed as $M_{F,s}$ as it is in terms of shaft power) and substituting for T .

$$P = \frac{W/N_P}{(M_{F,s})_{prop.}} \sqrt{\frac{W/N_P}{2\rho A_{x,prop.}}} \quad (1.7)$$

The thrust generated by a ducted fan using the same power can be found by rearranging Eqn. 1.1

$$T_{fan} = \left[(M_{F,s})_{fan} P \sqrt{2\rho A_{x,fan}} \right]^{\frac{2}{3}} \quad (1.8)$$

In order to perform better than a propeller, this thrust must be greater than the new total vehicle weight.

$$W + \Delta W < N_P \cdot T_{fan} \quad (1.9)$$

where ΔW is the extra weight of the vehicle due to the ducted fans. Combining Eqn. 1.8 and Eqn. 1.9

$$W + \Delta W < N_P \left[(M_{F,s})_{fan} P \sqrt{2\rho A_{x,fan}} \right]^{\frac{2}{3}} \quad (1.10)$$

Using the thrust = weight condition satisfied by the propeller in Eqn 1.7

$$W + \Delta W < \left[\frac{(M_{F,s})_{fan} \sqrt{A_{x,fan}}}{(M_{F,s})_{prop.} \sqrt{A_{x,prop.}}} \right]^{\frac{2}{3}} \cdot N_P \left[(M_{F,s})_{prop.} P \sqrt{2\rho A_{x,prop.}} \right]^{\frac{2}{3}} \quad (1.11)$$

The requirement for the ducted fan to perform better than the propeller is

$$\frac{W + \Delta W}{W} < \left[\frac{(M_{F,s})_{fan} \sqrt{A_{x,fan}}}{(M_{F,s})_{prop.} \sqrt{A_{x,prop.}}} \right]^{\frac{2}{3}} \quad (1.12)$$

Taking the theoretical figure of merit for the fan ($M_{F,s} = \sqrt{2\sigma}$) and propeller ($M_{F,s} = 1$) this becomes simply

$$\frac{W + \Delta W}{W} < \left[2\sigma \frac{A_{x,fan}}{A_{x,prop.}} \right]^{\frac{1}{3}} \quad (1.13)$$

where $W + \Delta W$ is the total weight of the flying test bed and ducted fans. The difference between the right hand side (RHS) and left hand side (LHS) of Eqn. 1.13 gives the change in fan weight required to satisfy the inequality as a percentage of payload.

$$\Sigma = \left[2\sigma \frac{A_{x,fan}}{A_{x,prop.}} \right]^{\frac{1}{3}} - \frac{W + \Delta W}{W} \quad (1.14)$$

This is referred to as the “superiority parameter” as any design that gives a value of $\Sigma > 0$ will require less power to maintain hover than an ideal propeller of a specified size, and hence have superior performance. Equation 1.14 provides two explicit design objectives:

1. Exit duct exit area should be maximised ($A_e = \sigma A_x$);
2. Ducted fan weight should be minimised

Exit area, A_e , can be increased by increasing flow area, A_x , and increasing the area ratio, σ . Both result in an increase in propulsor mass: a larger flow area requires a larger fan and casing; and larger area ratios ($\sigma > 1$) increase diffusion in the exit duct (to prevent the diffuser from separating due to adverse pressure gradients, the length of diffuser must scale with the area ratio). A mass model is required to estimate propulsor weight for a given design point, allowing the superiority parameter to be evaluated.

1.2.1 Design Context

In this report, ducted fan design is constrained by available manufacturing techniques (3D printing on Ultimaker 3). This introduces physical limits on the maximum size of propulsor

that can be manufactured and tested¹. The size of the build plate limits the maximum outer diameter of the propulsor to 185mm. The vertical length of components is limited to 200mm by the vertical travel of the build plate.

Given a fixed payload ($\approx 1\text{kg}$), Eqn. 1.13 suggests the superiority condition could be satisfied provided a light and large enough fan can be produced, and this is explored in the design section. The size required for the superiority condition to be satisfied can only be determined once a suitable mass model is developed.

1.3 Research Question

The research question proposed for this project is:

Does a vehicle with a ducted fan propulsor consume less power to maintain hover than a propeller?

The size of the design space highlights the importance of a systems approach to the problem due to its multi-disciplinary nature. The question is broken down into 3 sub-questions.

1. Can a figure of merit of $M_{F,s} > \sqrt{2}$ be achieved using an exit duct area ratio of $\sigma > 1$?
2. For a specific application and design context, can the superiority condition be satisfied?
3. Can in-flight performance be predicted by stationary tests?

These questions require a suitable platform to be developed to enable comparison of in-flight and stationary performance, as well as provide the design context and specific application required for the ducted fan design process. Performance is to be compared to a 10 inch Advanced Performance Composites (APC) 10×4.7 ‘Slow Flyer’ (VTOL optimised) propeller, as the manufacturer provides calibration and performance data^[8] that is supported by experiment^[9].

¹In a general application, size limits still apply and propulsor design is therefore constrained accordingly.

2 Flying Test Bed System Design

The flying test bed (see Fig. 2.1) is a system developed to enable testing of propulsors in a realistic environment. Its roles are to manage data collection and power supply during stationary tests, and control vehicle dynamics and collect data during hover tests.

2.1 Flying Test Bed

A UROP was conducted in the summer preceding this project during which an axi-symmetric quadcopter-configuration flying test bed was designed and manufactured. The two challenges addressed were structural design of the chassis, and the customisation of flight control hardware and software. The UROP concluded with successful flight of the flying test bed using “off-the-shelf” 10in. propellers. In this report, the flying test bed is updated allowing measurements to be taken using both propellers and ducted fans in stationary test and hover test configurations.

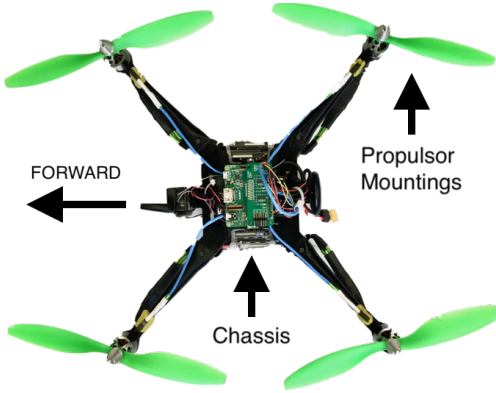


Figure 2.1: Plan view of flying test bed with propellers attached

2.1.1 Mechanical and Electrical Design

The test bed is designed to be 3D printable, light weight yet stiff, and modular to allow various propulsors and instrumentation to be mounted, as well as allowing for design iteration and part replacement if required. Instrument management systems and flight hardware are mounted on a chassis that is printed as one piece for rigidity and to reduce complexity. Cantilevered propulsor arms are attached to the central chassis with a double mortise and tenon style mount, and fastened as shown in Fig. 2.2.

The flying test bed chassis has dimensions of approximately $125mm \times 139mm \times 93mm$. It has a dry mass (excluding battery) of $0.529kg$ and the battery has a mass of $0.466kg$. The following hardware is mounted directly onto the chassis:

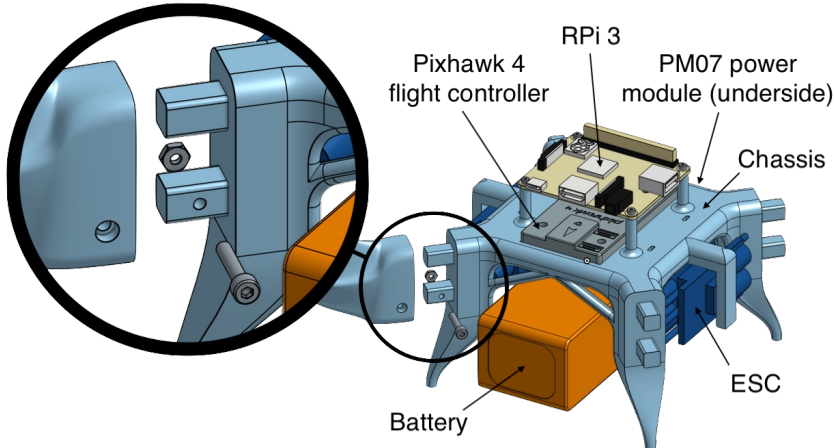


Figure 2.2: Flying test bed chassis showing exploded detail of double mortise and tenon joint for propulsor arms

Pixhawk 4 flight controller	Packaged, customizable autopilot hardware
Raspberry Pi 3 Model A+ (RPi3)	RPi3 provides on-board data capture and instrument management, allowing remote collection of thrust and RPM data streams using custom Python code. The RPi3 is accessed wirelessly via secure shell (SSH) and secure copy protocol (SCP)
ADCPi ADC breakout	Stackable analogue to digital converter (ADC) mounted directly to the Raspberry Pi 3
PM07 power module	Power module manages regulated 5V power supply for the Pixhawk 4 and RPi3 from inputs of 7-51V. High power outputs provide up to 30A to each motor
Aerostar 50A ESC	(4x) Electronic speed controller driving BLDCM motors
Turnigy Li-Po Battery	5000 mAh capacity 4-cell (14.8V nominal) battery. Can be replaced by a tethered 12V power supply

2.1.2 Flight Controller Customisation

The Pixhawk 4 flight controller manages flight dynamics and motor control. In order for steady static hover to be achieved, the PID control system gains are tuned to match the flying test bed weight and configuration. Small corrective inputs are required from the operator to ensure stationary hover in enclosed environments due to wall effects.

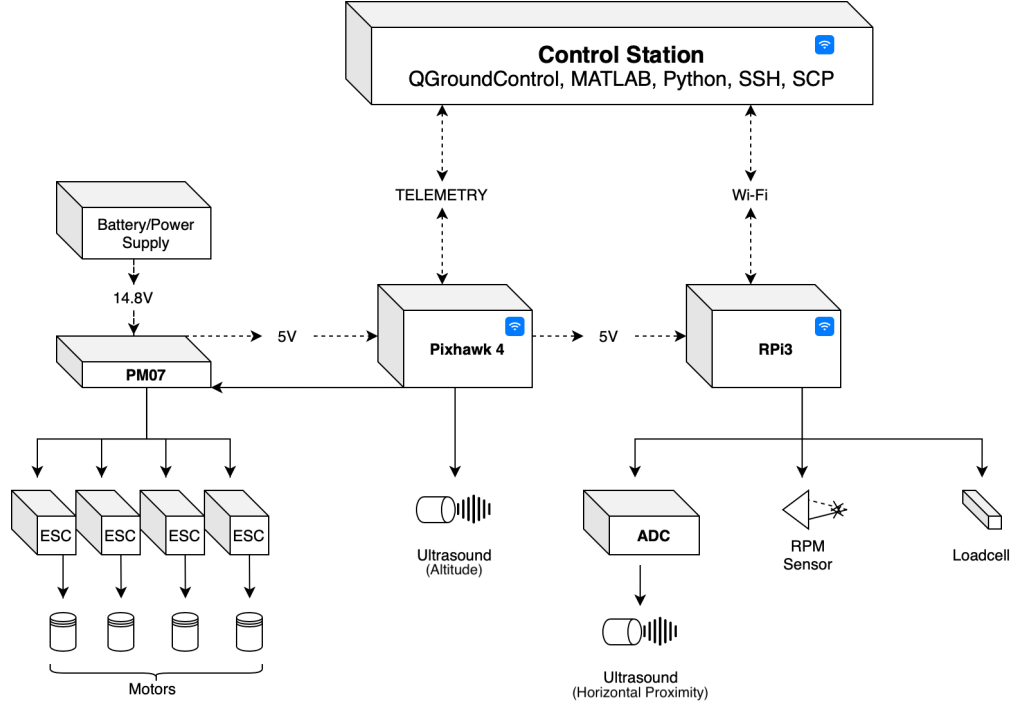


Figure 2.3: Subsystem schematic of flying test bed

2.1.3 Subsystem Interaction

All positional, power, and control subsystems are managed by the Pixhawk 4. This includes 3 ultrasound sensors for altitude (z) and horizontal proximity (x, y). Wireless telemetry modules allow data transfer between the Pixhawk 4 and the control station, and a Wi-Fi router connects the RPi3 to the control station. Power usage data is transferred via telemetry. Thrust and RPM data is transferred using SCP over Wi-Fi. Figure 2.3 shows schematically how the subsystems interact.

3 Ducted Fan Aerodynamic Design

3.1 Introduction

This section describes the aerodynamic design of an electric ducted fan designed to replace a propeller on a VTOL electric vehicle. The flying test bed is powered by 4 propulsors and is designed to achieve steady hover with a payload equal to the weight of the flying test bed. The ducted fans are to be 3D printed in PLA. The design process is summarised by the flow chart in Fig. 3.1. Low Reynolds number blade profiles from Maffioli *et al.*^[10] are used in the design.

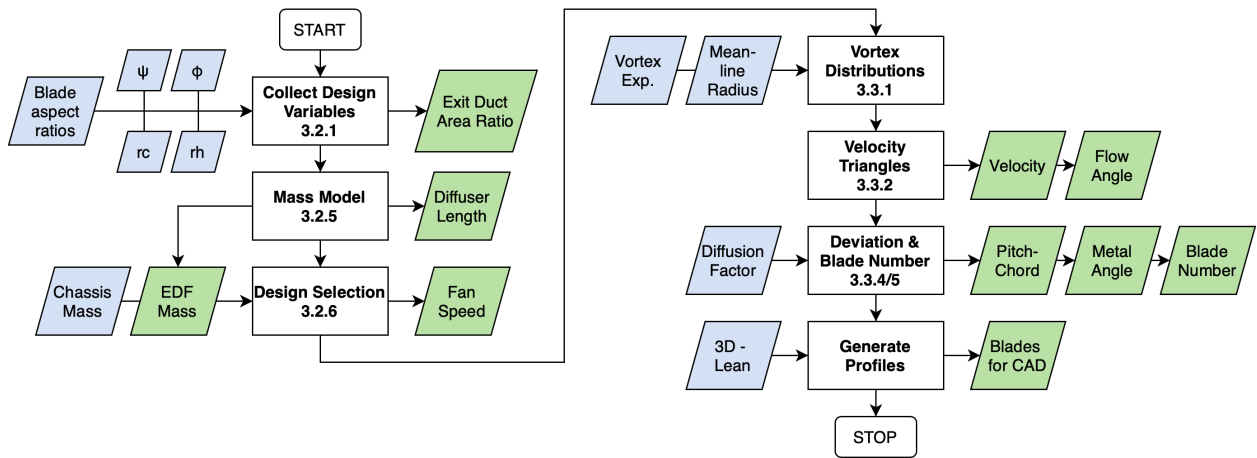


Figure 3.1: Flow chart showing the aerodynamic design process. 2D design stages are on the left and the 3D design stages are on the right. Processes are labelled by the report section in which they appear (3.x.x)

3.2 Mean-line Design

The propulsor design at mean-line determines overall performance of the ducted fan. The choice of mean-line location for a low hub-to-tip ratio (HTR) machine is discussed and validated.

3.2.1 Non-dimensional Operating Point

Blade design is determined by the choice of non-dimensional operating point, given by flow coefficient, ϕ , and stage loading, ψ

$$\phi = \frac{V_x}{U} \quad (a) \qquad \psi = \frac{\Delta h_0}{U^2} \quad (b) \qquad (3.1)$$

where the mean-line blade velocity is $U = \Omega \cdot r_m$ with fan angular velocity, Ω , and mean-line radius, r_m , and Δh_0 is the change in stagnation enthalpy across the fan. Assuming isentropic flow, stage loading can be written in terms of the stagnation pressure rise, Δp_0 . Using Bernoulli's equation and assuming exit static pressure, p_e , is equal to atmospheric static pressure, $p_{atm.}$, Δh_0 can be expressed in terms of axial blade passage velocity V_x and exit duct area ratio, σ .

$$\Delta h_0 = \frac{\Delta p_0}{\rho} \quad (3.2)$$

$$\Delta p_0 = (p_0)_e - (p_0)_{in} = \left(\frac{1}{2}\rho V_e^2 + p_e\right) - p_{atm.}$$

$$\Delta p_0 = \frac{1}{2}\rho V_e^2 \implies \Delta h_0 = \frac{V_x^2}{2\sigma^2} \quad (3.3)$$

$$\therefore \psi = \frac{V_x^2}{U^2} \cdot \frac{1}{2\sigma^2} \quad (3.4)$$

Therefore ϕ , ψ , and σ are related by

$$\psi = \frac{\phi^2}{2\sigma^2} \quad (3.5)$$

The operating point can therefore be defined by the mean-line flow coefficient, ϕ_m , and mean-line stage loading, ψ_m . This allows the resulting figure of merit to be determined from Eqn. 1.6.

3.2.2 Fan Operating Speed

The fan speed is determined by the magnitude of thrust required, shown by substituting Eqn. 3.1a into Eqn. 1.4.

$$\Omega = \frac{1}{r_m \phi_m} \sqrt{\frac{T\sigma}{\rho A_x}} \quad (3.6)$$

This shows fan speed to vary with both thrust and fan size, and so the required fan speed can only be evaluated once a suitable mass model has been determined.

3.2.3 Mean-line Location

Maximising the flow area for a given propulsor radius maximises thrust developed (see Eqn. 3.6) and ensures minimum use of material and therefore a lighter design. This results in a small hub radius (limited only by electric motor size, typically $> 15\text{mm}$) and consequently

low hub-to-tip (HTR) ratios (< 0.5). Selecting a mean-line location at the mid-span radius gives different mass flows above and below the mean-line, resulting in variation in loading across the span. An alternative mean-line position is defined by balancing the flow area above and below the mean-line, setting the mean-line radius at the root-mean-square (RMS) of the hub and casing radii.

$$r_m = \sqrt{\frac{r_h^2 + r_c^2}{2}} \quad (3.7)$$

3.2.4 Overall Performance

Expressions for fan thrust and power can now be determined in terms of the non-dimensional operating point and the fan's geometric variables.

$$T = \frac{\rho\pi\phi_m^2\Omega^2(r_c^4 - r_h^4)}{2\sigma} \quad (3.8)$$

$$P = \frac{\rho\pi\phi_m^3\Omega^3(r_c^2 - r_h^2)}{2\sigma^2} \left(\frac{r_c^2 + r_h^2}{2} \right)^{\frac{3}{2}} \quad (3.9)$$

3.2.5 Mass Model

In order to solve the superiority condition and determine required fan speed, a mass model is needed to relate estimated propulsor weight to its design variables. Figure 3.2 shows an exploded view of the components making up the mass model. The diffuser hub, diffuser casing, and the intake are modelled as hollow truncated cones. The blade duct hub and casing are modelled as hollow cylinders. Blade rows are modelled as thin annular disks. All parts are 3D printed in PLA.

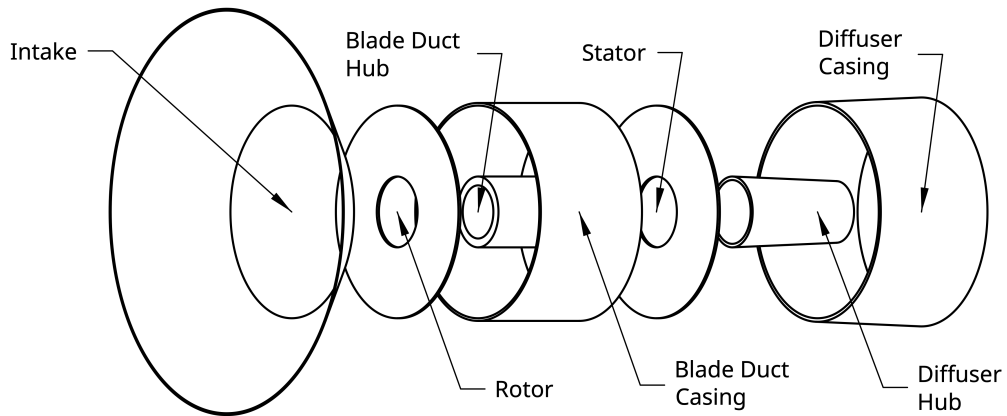


Figure 3.2: Exploded view of ducted fan mass model components

Diffuser The length of diffuser required to prevent flow separation increases as diffuser area ratio increases. ESDU 75026^[11] discusses the performance of symmetric annular diffusers in incompressible flows and presents empirical limits of separation at various length and area ratios. By evaluating the design static pressure recovery coefficient, the required diffuser length to avoid separation can be determined. Considering Eqn. 1.3 and Bernoulli's equation, static pressure recovery can be written as

$$C_{pr} = \frac{p_e - p_x}{\frac{1}{2}\rho V_x^2} = 1 - \frac{1}{\sigma^2} \quad (3.10)$$

where p_x is the static pressure at entry to the exit duct. ESDU 75026 shows two length limits, C_{pr}^* and C_{pr}^{**} , in terms of required area ratio, representing the diffuser separation limit (C_{pr}^*) and the limit of performance due to frictional loss and boundary layer growth (C_{pr}^{**}). Designing close to C_{pr}^{**} will produce a diffuser that is unlikely to separate. This line can be approximated with an R-squared value of 0.9999 by

$$\frac{L_{diff.}}{r_c - r_h} = -5.56\sigma^3 + 24.16\sigma^2 - 23.41\sigma + 5.413 \quad (3.11)$$

The diffuser hub and casing are modelled as hollow truncated cones with height $L_{diff.}$ (determined by Eqn. 3.11), a base radius r_h (for the hub) and $(r_c)_{exit}$ (for the casing), a truncation radius of $(r_h)_{exit}$ (for the hub) and r_c for the casing, and a thickness t . Diffuser exit hub and casing radius for a symmetric diffuser can be found by considering an equal flow angle at the hub and casing giving

$$\frac{(r_c)_{exit} - r_c}{L} = \frac{r_h - (r_h)_{exit}}{L} \quad (3.12)$$

$$\therefore (r_c)_{exit}, (r_h)_{exit} = \frac{r_c + r_h}{2} \pm \frac{\sigma}{2}(r_c - r_h) \quad (3.13)$$

The volume of a hollow truncated cone, using the variables defined in Table 3.1, allows the total mass of the diffuser to be determined.

$$V = \frac{h\pi}{3}(R^2 + Rr + r^2 - S^2 - Ss - s^2) \quad (3.14)$$

$$m_{diff.} = \rho_{PLA}(V_{hub} + V_{case}) \quad (3.15)$$

Blade Passage The blade passage (excluding rotor and stator blades) is modelled as a straight annulus. The passage itself has inner radius r_h and outer radius r_c . The casing is modelled to have thickness of $t_c = 1.5mm$ and the hub section has a thickness of $t_h = 5mm$. The length of the blade passage is estimated as $L_{BP} = 70mm$ giving a total mass

$$m_{BP} = 2.73r_h + 0.818r_c - 0.0062 \quad (3.16)$$

	Hub value	Casing value
R	r_h	$(r_c)_{exit} + t$
r	$(r_h)_{exit}$	$r_c + t$
S	$r_h - t$	$(r_c)_{exit}$
s	$(r_h)_{exit} - t$	r_c
h	$L_{diff.}$	$L_{diff.}$

Table 3.1: Parameter values for diffuser hub and casing

Intake The intake is modelled as a hollow truncated cone, an approximation for its actual ellipsoidal cross-section. Its length is equal to the difference between its inner and outer radius, given by $\Delta r = 0.5r_c$. Eqn. 3.14 gives an approximate intake mass assuming a thickness of 1mm.

$$m_{in.} = 3.90(r_c - r_h)(3r_c - r_h + 0.001) \quad (3.17)$$

Blades The blades are modelled as having the equivalent mass of an annular flat disk of thickness $t_{rotor} = 1.5\text{mm}$ for the rotor and $t_{stator} = 1.5\text{mm}$ for the stator. The resulting mass is given by

$$m_{blades} = 11.7(r_c^2 - r_h^2) \quad (3.18)$$

Thrust–Weight Balance In hover, propulsor thrust is equal to its share of the total vehicle weight. The payload here is the flying test bed chassis. The required thrust for each propulsor can be expressed in terms of the mass model components and the number of propulsors, N_P .

$$m_{fan} = m_{diff.} + m_{BP} + m_{in.} + m_{blades} + m_{motor} \quad (3.19)$$

$$T = g \left[m_{fan} + \frac{m_{chassis}}{N_P} + \frac{m_{battery}}{N_P} \right] \quad (3.20)$$

3.2.6 Design Selection

The following constraints and objectives are imposed on the design space. They are considered in the following order:

1. Design in a high efficiency region for low Reynolds number blade profiles (Maffioli *et al.*^[10])
 - Choose operating point for ϕ_m and ψ_m , hence determine σ
2. Satisfy the superiority condition (Eqn. 1.13)

- Minimise propulsor mass
 - Maximise flow area and exit duct area ratio
 - Choose geometric design point for r_c and HTR
3. Operate in a suitable speed-torque regime for the electric motor
- Calculate operating point for Ω based on T , σ , and ϕ_m as in Eqn. 3.6

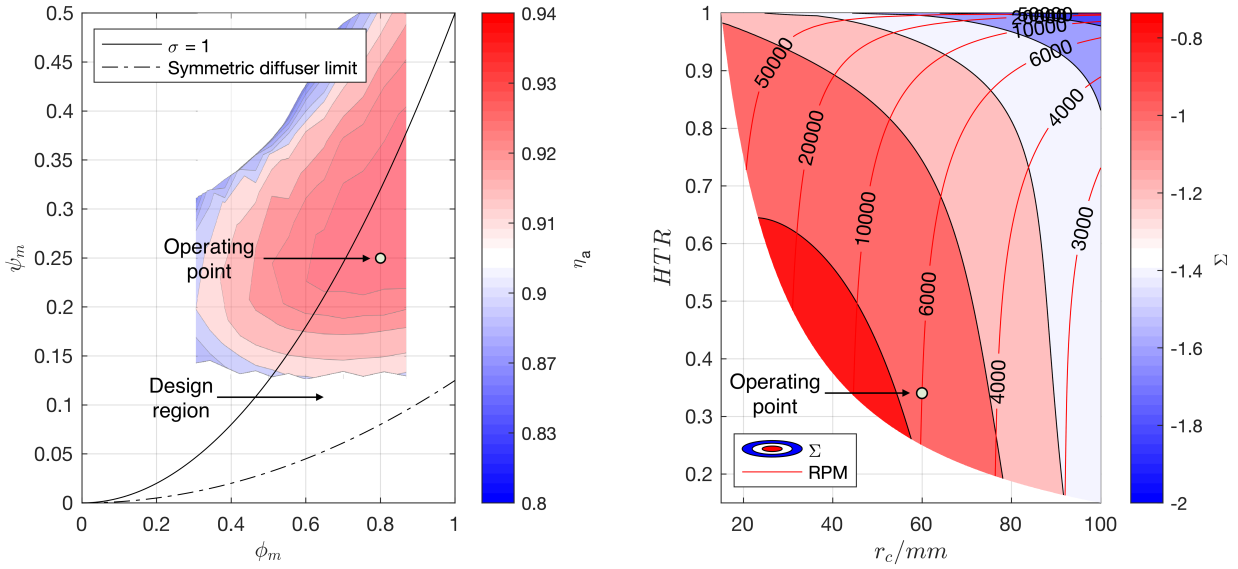
The resulting design point is shown in Table 3.2.

Blade Operating Point Figure 3.3a shows a Smith chart for the Maffioli *et al.*^[10] low Reynolds number ($Re \approx 50,000$) blade profiles used in this design, overlaid on the ϕ_m - ψ_m design space. The design region lies between the limit of $\sigma = 1$, required to obtain a design figure of merit of $M_F > \sqrt{2}$ (solid line), as well as a symmetric diffuser limit arising from the diffuser hub converging to a point (dashed line).

The Smith chart contours show that blade efficiency in a 2D cascade decreases for flow coefficients $\phi_m < 0.6$ and stage loading $\psi_m < 0.2$. This is verified by Corralejo *et al.*^[12]. The operating point of $\phi_m = 0.8$, $\psi_m = 0.25$ is chosen as it lies in the middle of a high efficiency region of the design space, as marked on Fig. 3.3a. This gives an exit duct area ratio of $\sigma = 1.1314$.

Geometric Design Point Using the mass model, the superiority condition is determined in terms of the free variables r_c and HTR ($HTR = r_h/r_c$) for $\sigma = 1.1314$, a fixed propeller area $A_{x,prop.}$, and assumed ideal propeller figure of merit as in $((M_{F,s})_{prop.} = 1)$. As discussed in Section 1.2.1, maximum propulsor radius is limited by manufacturing methods and minimum hub radius is determined by the size of the electric motor (typically $r_h > 15\text{mm}$) and so the design space explored is defined by $15\text{mm} \leq r_c \leq 100\text{mm}$ and a HTR range of $0 \rightarrow 1$ (provided $r_h > 15\text{mm}$). Figure 3.3b shows the value of the superiority parameter, Σ (see Eqn. 1.14), which must be positive for the superiority condition to be satisfied.

Figure 3.3b shows that low values of Σ are observed at high HTR. Increasing HTR reduces the flow area and the ratio $A_{x,fan}/A_{x,prop.}$. The reduction in ΔW resulting from a smaller fan is outweighed by the reduction in $A_{x,fan}/A_{x,prop.}$, hence reducing Σ . Figure 3.3b shows Σ to be negative throughout this design region, meaning the superiority condition is not satisfied. At larger payloads, and through the use of advanced materials, the ratio of $\Delta W/W$ decreases allowing the condition to be satisfied. This is explored in Section 6. Therefore, a design that does not satisfy the superiority condition but achieves $M_F > \sqrt{2}$ is chosen. The superiority parameter is maximised at low values of r_c and low values of HTR. As r_c decreases, the motor speed required to maintain sufficient thrust for hover increases rapidly, as shown by the contours of RPM in Fig. 3.3b. A casing radius of 60mm and a HTR



(a) Blade operating point design space shown with exit duct area ratio limits and Maffioli (2015) Smith chart overlaid. Note non-linear color bar

(b) Superiority condition across the r_c -HTR geometric design space. Contours of RPM required to maintain hover are overlaid

Figure 3.3: Blade aerodynamic and propulsor geometric design spaces

of $1/3$ is chosen, giving a hub radius of 20mm and a predicted $\Sigma = -0.84$.

Electric Motor Operating Point The mass model is used to estimate the weight of the ducted fan propelled vehicle, and therefore determine the thrust required ($T = W/N_P$). Equation 3.8 is used to calculate the rotor speed required to achieve this thrust, and RPM contours are plotted on Fig. 3.3b.

$$\Omega = \sqrt{\frac{2\sigma \frac{W}{N_P}}{\rho \pi \phi_m^2 (r_c^4 - r_h^4)}} \quad (3.21)$$

At the chosen design point this gives a motor speed of

$$\therefore \Omega = 627.5 \text{ rad} \cdot \text{s}^{-1} = 5992 \text{ RPM} \approx 6000 \text{ RPM} \quad (3.22)$$

Velocity Triangles Now the design parameters have been determined, the mean-line velocity triangles can be drawn for this particular design. Figure 3.4 shows the velocity triangles in context with rotor and stator blades. Flow angles are measured as positive in the sense of rotor rotation (in Fig. 3.4 this is positive down).

ϕ_m	0.80
ψ_m	0.25
σ	1.1314
$L_{diff.}$	72.0mm
r_c	60mm
r_h	20mm
r_m	44.7mm (RMS)
Ω	6000 RPM

Table 3.2: Propulsor design point

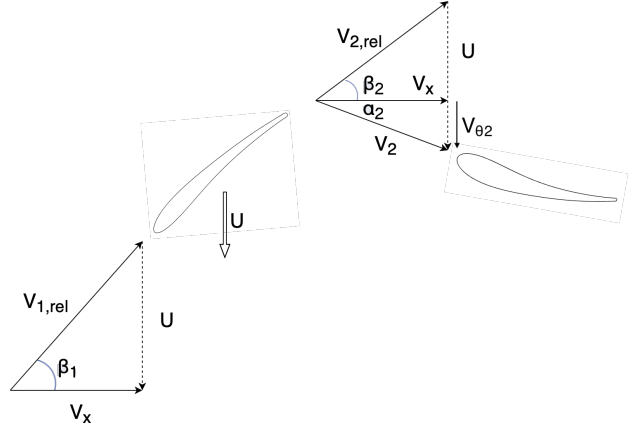


Figure 3.4: Mean-line velocity triangles (stator exit omitted as flow axial at exit)

3.3 3D Blade Design

Overall performance has been determined by setting the mean-line values of flow coefficient, ϕ_m , and stage loading, ψ_m . The values of ϕ and ψ must vary along the span as radial equilibrium must be maintained across the span.

3.3.1 3-dimensional Flow Solutions to Radial Equilibrium

Radial equilibrium states that for axi-symmetric and incompressible annulus flow Eqn. 3.23 must be satisfied.

$$\frac{dh_0}{dr} - T \frac{ds}{dr} = V_x \frac{dV_x}{dr} + \frac{V_\theta}{r} \frac{d(rV_\theta)}{dr} \quad (3.23)$$

Assuming there is no variation in stagnation enthalpy or entropy across the span, this reduces to

$$V_x \frac{dV_x}{dr} + \frac{V_\theta}{r} \frac{d(rV_\theta)}{dr} = 0 \quad (3.24)$$

Noting Eqn. 3.1 and applying Euler's work equation, we obtain

$$\phi r \frac{d(\phi r)}{dr} + \psi \frac{d(\psi r^2)}{dr} = 0 \quad (3.25)$$

Which has general solutions in the form

$$\phi = \phi_m \left(\frac{r}{r_m} \right)^A \quad (a) \qquad \psi = \psi_m \left(\frac{r}{r_m} \right)^B \quad (b) \quad (3.26)$$

Substituting Eqn. 3.26a and Eqn. 3.26b into Eqn. 3.25 gives

$$\left[\phi_m \left(\frac{r}{r_m} \right)^A \right]^2 (1 + A) = - \left[\psi_m \left(\frac{r}{r_m} \right)^B \right]^2 (2 + B)$$

$$\therefore \phi^2 (1 + A) = -\psi^2 (2 + B) \quad (3.27)$$

This solution is used to determine the values of the constants A and B , where B is referred to here as the vortex distribution exponent as it determines the tangential velocity variation in the r - θ plane.

Free Vortex ($B = -2$) One such distribution arises from the free vortex condition. This results from the solution to Eqn. 3.27 in which both LHS and RHS are equal to zero giving

$$A = -1 \quad (a) \qquad \qquad B = -2 \quad (b) \quad (3.28)$$

Therefore from Eqn. 3.26a and Eqn. 3.28a

$$\phi(r) \sim \frac{1}{r} \qquad \qquad \therefore \frac{d}{dr}(V_x) = 0 \quad (3.29)$$

It can be shown from Eqn. 3.26b and Eqn. 3.28b

$$\psi(r) \sim \frac{1}{r^2} \qquad \qquad \therefore \frac{d}{dr}(\Delta h_0) = 0 \quad (3.30)$$

Therefore axial velocity and loading are constant across the span. The result is a theoretically vorticity free flow^[13]. Constant V_x and constant Δh_0 conditions indicate uniform exit static pressure. In practice the variation in $V_{\theta 2}$ across the span results in large variations in blade twist angle that should be avoided (see Fig. 3.5 that shows $V_{\theta 2}$ variation resulting in over 20° of absolute flow angle variation). Furthermore, Fig. 3.5 shows stage loading, ψ , to become larger than 1 at radii close to the hub. From Euler's work equation, and given axial inlet flow

$$\Delta V_\theta = V_{\theta 2} = \psi U \quad (3.31)$$

This shows the tangential velocity at the hub to be greater than the local blade speed. By reducing the value of B , this can be avoided by keeping $\psi_{hub} \leq 1$.

Mixed Vortex ($-2 \leq B \leq 0$) The radial equilibrium equation can be solved numerically, provided ϕ_m , ψ_m and r_m are known. The mixed vortex design shown in Fig. 3.5 has a vortex distribution exponent of $B = -1.7$. This produces a vortex distribution that, at the hub, has a tangential velocity equal to the local blade speed. This reduces the absolute velocity

of the flow past the wall and therefore reduces frictional loss at the hub. Hereafter, any reference to a ‘mixed vortex design’ corresponds to a vortex distribution exponent of $B = -1.7$.

Constant Angle Another common design is for constant absolute flow angle across the span, such that

$$\frac{d}{dr} \left(\frac{V_\theta}{V_x} \right) = 0 \quad (3.32)$$

$$\therefore \frac{\psi}{\phi} = \text{constant} \left(= \frac{\psi_m}{\phi_m} \right) \quad (3.33)$$

This results in the exponents A and B being equal giving

$$A = B = - \left(\frac{2\psi_m^2 + \phi_m^2}{\psi_m^2 + \phi_m^2} \right) \quad (3.34)$$

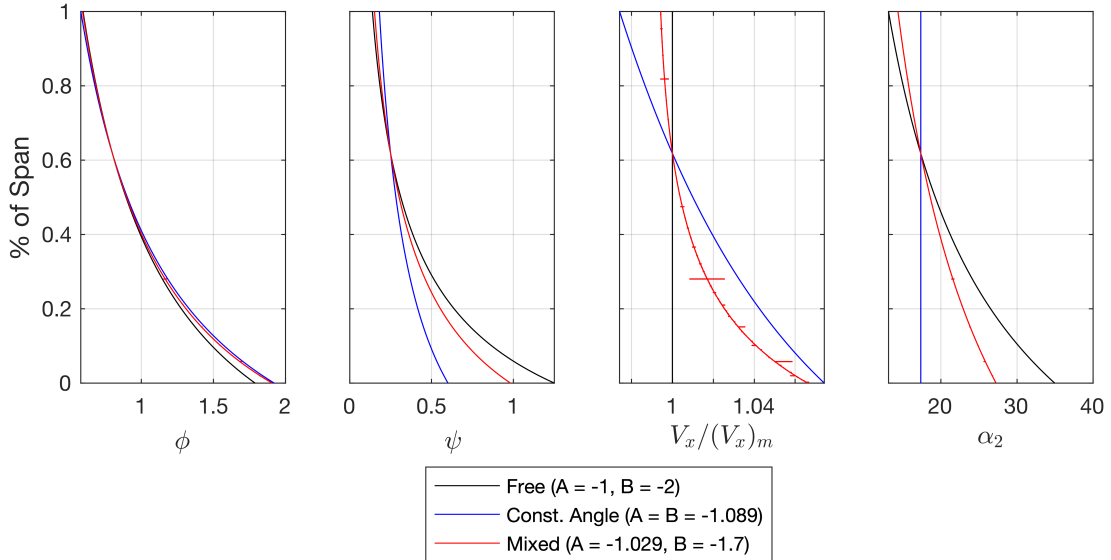


Figure 3.5: Distributions of design parameters ϕ and ψ and non-dimensionalised axial and tangential velocities, V_x and $V_{\theta 2}$ (shown using α_2) respectively, across the span for 3 different vortex designs (free vortex, constant angle and mixed vortex)

3.3.2 3D Velocity Triangles

Once the distributions of ϕ and ψ have been determined, the variation in flow velocities and angles across the span can be found. The relative merits of each of the vortex distributions are discussed in Section 6, in which the three designs presented here are tested.

3.3.3 Validation of Mean-line Location

Eqn. 3.8 and Eqn. 3.9 result from the assumption that mean-line design parameters are representative of the performance of the whole flow. This assumption is now verified as span-wise distribution of the flow parameters ϕ and ψ are determined. Integrating the work done and thrust generated by an infinitesimal annular element, the integral power and thrust produced by the propulsor is evaluated. This is computed numerically for each vortex design.

$$P = \int_{r_h}^{r_c} \Delta h_0 \cdot d\dot{m} \quad (3.35)$$

$$\Delta h_0 = \psi U^2 \quad (a) \qquad d\dot{m} = \rho V_x (2\pi r dr) \quad (b) \quad (3.36)$$

$$\therefore P = 2\pi\rho\Omega^3 \cdot \frac{\phi_m \psi_m}{r_m^{B+A}} \int_{r_h}^{r_c} r^{A+B+3} dr \quad (3.37)$$

A similar expression can be obtained for integral thrust. The mass-averaged mean-line radius definition of r_m is compared to the conventional mean-line radius definition of r_m by calculating the error between the integral power and thrust, and that predicted from the mean-line design point. A properly balanced mean-line radius choice ensures the integral values are as close to the predicted ones as possible. Table 3.3 shows that selecting a mean-line radius at the RMS of the hub and casing radii reduces the error between the integral and the predicted power requirements to $\approx 1\%$. These errors are small enough to be neglected and so this choice of mean-line radius is validated.

Mean-line radius	P error	T error
$r_m = \text{mean}(r_c, r_h)$	37%	24%
$r_m = \text{RMS}(r_c, r_h)$	1.2%	0.36%

Table 3.3: Comparison of mean-line predicted and integral power and thrust from different mean-line definitions

3.3.4 Blade Number and Span-wise Chord

Lieblein *et al.*^[14] presents a correlation for diffusion factor as a function of velocities and the pitch-chord ratio of the blades.

$$DF = \left(1 - \frac{V_{2,rel}}{V_{1,rel}}\right) + \left(\frac{V_{\theta 1,rel} - V_{\theta 2,rel}}{2V_{1,rel}}\right) \frac{s}{c} \quad (3.38)$$

This expression is valid for both the rotor and stator, provided the relative reference frame values are taken for each blade. Pitch-chord across the span can be determined as

$$\frac{s}{c} = \left[DF - \left(1 - \frac{V_{2,rel}}{V_{1,rel}} \right) \right] \left(\frac{2V_{1,rel}}{V_{\theta 1,rel} - V_{\theta 2,rel}} \right) \quad (3.39)$$

The number of blades is determined using mean-line values. Mean-line chord, c_m , is estimated using the blade aspect ratio, $AR = l/c_m$, where blade span is $l = r_c - r_h$.

$$c_m = \frac{r_c - r_h}{AR} \quad (3.40)$$

$$N = \frac{2\pi r_m}{(s/c)_m c_m} \quad (3.41)$$

Similar blade numbers in the rotor and stator, or low common multiples of blade number, results in more blade interaction and higher acoustic output. Odd or prime numbers are selected to minimise interaction, provided this number is not too far from the calculated blade count. Table 3.4 outlines the calculated and selected blade numbers for each of the designs discussed. Using the blade number, the local chord can be determined using local pitch-chord ratio and radius

$$c = \frac{2\pi r}{(s/c)N} \quad (3.42)$$

The span-wise distribution of pitch-chord ratio is determined, provided a suitable diffusion factor is chosen. CUED Turbomachinery I^[15] presents a separation limit when $DF_{lim.} = 0.6$, and suggests $DF = 0.45$ as a suitable design point to avoid separation. The resulting chord distributions, for both the free and mixed vortex designs, are shown for the rotor in Fig. 3.6a (solid line).

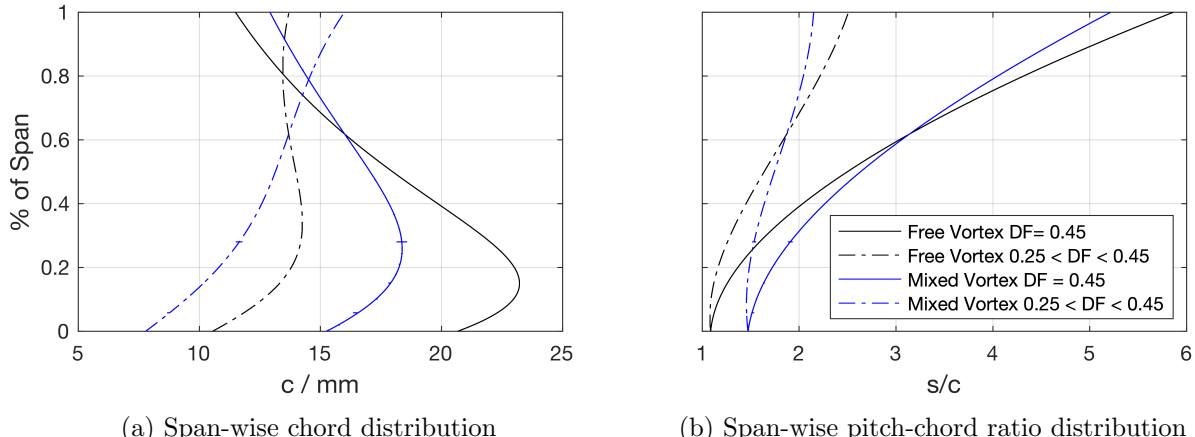


Figure 3.6: Span-wise distributions for the free and mixed vortex designs with constant diffusion factor and linearly varying diffusion factor

For the free vortex design the variation in chord across the span is large, with tip chord less than half the maximum chord. Changing to the mixed vortex condition reduces this variation significantly as tip chord increases and hub chord decreases. Large variations in pitch-chord ratio for the free vortex design (as in Fig. 3.6b) arises the tangential velocity component for the free vortex design varying across the span. Lieblein *et al.*^[14] shows an increase in loss for diffusion factors above 0.55 in the hub to mean-line region, and above 0.3 in the tip region. Therefore varying the diffusion factor across the span maintains a constant margin to Lieblein’s suggested limits. The dot-dashed lines in Fig. 3.6b show the pitch-chord ratio across the span with a diffusion factor varying linearly from 0.45 at the hub to 0.25 at the tip. This limits the variation in pitch-chord ratio across the span. Consistency in pitch-chord has further implications for deviation and is explored in the following section.

Vortex Design	Diffusion Factor	Rotor		Stator	
		N_R	Selected	N_S	Selected
Free, Mixed	$DF = 0.45$	(5.60)	7	(4.66)	5
	$0.25 \leq DF \leq 0.45$	(10.48)	11	(7.20)	7

Table 3.4: Rotor and stator blade numbers at various design conditions. Blade numbers based on midline values so all vortex designs have equal N

3.3.5 Deviation

Flow deviation is estimated from correlations proposed by Howell (1945, 1)^[16], (1945, 2)^[17], and Carter (1950)^[18]. Commonly referred to as Carter’s rule it states that for a compressor blade

$$\delta = m_\delta \theta \sqrt{\frac{s}{c}} \quad (3.43)$$

where θ is the flow turning achieved in the relative frame, and m_δ is an empirically determined variable that can be approximated by

$$m_\delta = 0.23 \left(\frac{2a}{l} \right)^2 + \frac{\beta_2}{500} \quad (3.44)$$

where for a circular arc camber line $a/l = 0.5$. Hence the deviation varies $\sim \sqrt{s/c}$. Figure 3.7a shows the large increase in deviation angle at the rotor tips for both the free and the mixed vortex conditions when a constant diffusion factor is used (solid lines). Introducing a varying diffusion factor (dot-dashed lines) across the span results in reduced deviation due to reduced variation in pitch-chord ratio (Fig. 3.6b). Carter’s rule is derived from empirical results obtained from compressor cascades ($HTR \approx 1$). Care must be taken when applying

it to blades with large span-wise variations in pitch-chord ratio. A varying diffusion factor reduces the range of pitch-chord ratio significantly and Carter's rule predicts lower deviation angles. Consequently the variation in rotor exit metal angle is more consistent, as in Fig. 3.7b.

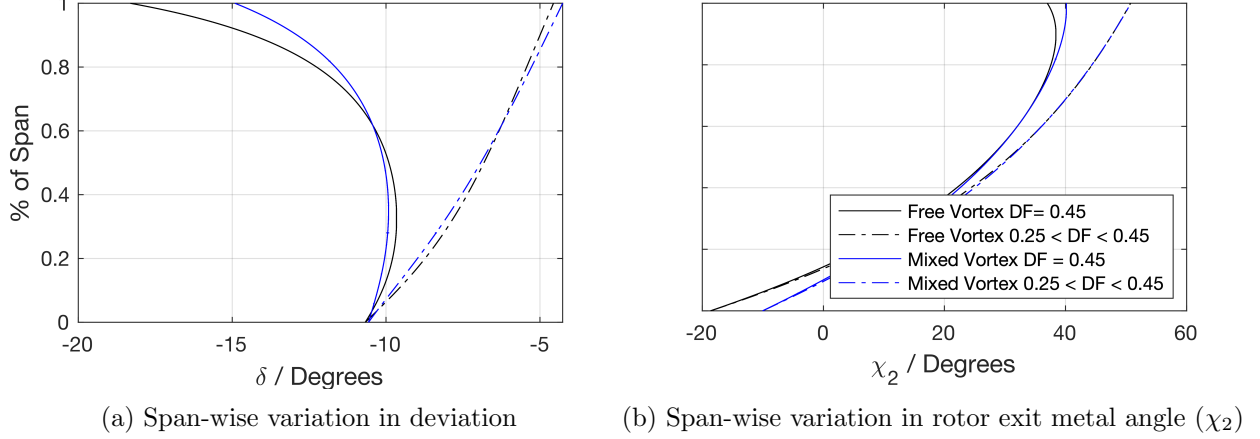


Figure 3.7: Span-wise distributions are shown for both the free and mixed vortex conditions (black and blue lines respectively) at both constant diffusion factor and linearly varying diffusion factor

3.3.6 Blade Lean

Taylor & Miller^[19] shows the limits of using a 2-dimensional design with respect to 3-dimensional flow. Ensuring the blade suction surface subtends the hub and casing at an obtuse angle helps reduce corner separations and trailing edge losses. Lean is added to the rotor and stator blades to satisfy this requirement. The rotor has 10° of lean at the hub and approximately 40° at the tip and the stator follows a parabolic lean profile with 10° of lean at the hub and tip.

4 Electrical and Mechanical Design

4.1 Introduction

The electrical and mechanical design is considered with respect to the determined operating point. The electric motor and power supply are chosen to be compatible with both the fan operating point, and the control system architecture.

4.2 Electrical Design

4.2.1 Power Supply

A 12V/84A (1kW) DC power supply is used to power the stationary propulsor tests and can be used in conjunction with a tether to provide flight power for hover tests. The flying test bed can optionally hold a 14.8V Li-Po enabling untethered testing. Due to its lower power output, the 12V power supply is used to determine the motor requirements.

4.2.2 Motor Requirements

Required motor speed is 6000 RPM giving a required isentropic power of $P_s = 54.4$ W. Shaft torque is $\tau_s = P_s/\Omega = 0.0867$ Nm assuming isentropic flow, no electrical losses from the motor and no windage and other frictional losses. The delay between a dynamic vehicle disturbance and the control system response, known as the control latency, should be minimised to increase stability meaning motor torque must be sufficient. Reducing control latency decreases data noise, as the power requirement from the motors is more stable (fewer changes in demand speed). The moment of inertia of the rotor about it's rotation axis is $I_{ZZ} = 51.01 \text{ kg}\cdot\text{mm}^2$, determined from a mass analysis of a CAD model of the rotor. The angular acceleration of the rotor is given by

$$I_{ZZ}\dot{\Omega} + \frac{\tau_s}{\eta_a} = \tau_e \quad (4.1)$$

where η_a is the aerodynamic efficiency. Taking τ_s as constant and equal to the value obtained above, the required motor torque, τ_e for a given angular acceleration of the shaft is equal to

$$\tau_e = 51.01 \times 10^{-6} \cdot \dot{\Omega} + \frac{0.0867}{\eta_a} \quad (4.2)$$

4.2.3 Choice of Electric Motor

A brushless DC motor (BLDCM) is modelled by the circuit in Fig. 4.1. The back-emf generated by the motor is proportional to the motor speed (as in Fig. 4.1) and the torque

produced is proportional to the current. Given that the torque constant, k_t , and voltage constant, k_v , are related by $k_t = 1/k_v \implies \tau_e = 3k_t I_{phase} = \frac{\sqrt{3}I_{supply}}{k_v}$. The motor speed can be related to the electrical input quantities by

$$Voltage = IR + E \implies Voltage = \left(\frac{\tau_e k_v}{\sqrt{3}} \right) R + \Omega k_v \quad (4.3)$$

$$\therefore \Omega = \left(Voltage - \frac{\tau_e k_v}{\sqrt{3}} R \right) \cdot k_v \quad (4.4)$$

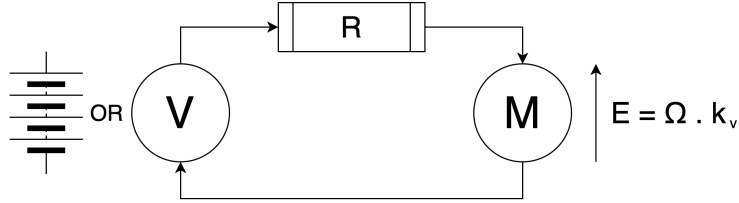


Figure 4.1: Electric motor model for DC/BLDC motors

Assuming linear acceleration from rest to demand speed ($\dot{\Omega}_{max}$) and a maximum acceleration time of $75ms$, Eqn. 4.2 gives a maximum motor torque requirement of $\tau_e = 0.428 + 0.0867/\eta_a$ Nm. The motor is required to have an outer diameter no greater than $30mm$ to fit inside the hub with hub radius $r_h = 20mm$ and wall thickness of $5mm$. These requirements are met by a Multistar Elite 2810-750kv BLDCM with internal resistance of 0.108 ohms and voltage constant of $750 \text{ RPM} \cdot \text{V}^{-1}$. Rearranging Eqn. 4.4 gives the output torque at 6000 RPM

$$\tau_e = 0.76 \text{Nm} \quad (4.5)$$

This enables a maximum acceleration of $\dot{\Omega}_{max} = 8400 \text{ rad}\cdot\text{s}^{-2}$, given an aerodynamic efficiency $\eta_a > 30\%$.

4.3 Mechanical Design

In this section the propulsor design is embodied and the mechanical aspects of the design considered. The propulsors positioned diagonally opposite from each other spin in one sense and those on the other diagonal spin in the other sense. This gives the flying test bed yaw control. As a result two versions of the propulsor are produced, one spinning clockwise and the other anti-clockwise. These are simple mirror images of each other and are not discussed further.

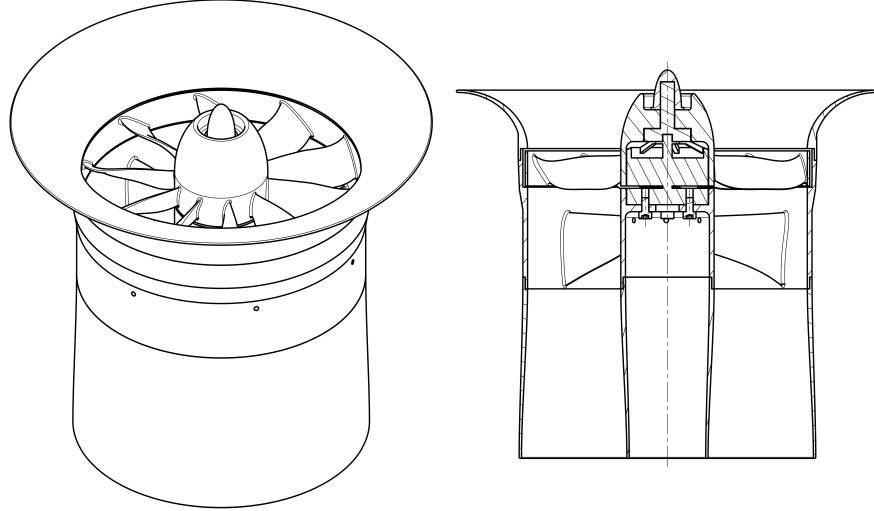


Figure 4.2: Isometric and section view of ducted fan design

4.3.1 Propulsor Dimensions

Rotor and stator blades have a total axial chord of 52.5mm including a 12mm blade row gap. A blade duct length of $L = 60\text{mm}$ is chosen. Equation 3.13 gives values of $(r_c)_{exit} = 62.6\text{mm}$ and $(r_h)_{exit} = 17.4\text{mm}$. Figure 4.2 shows an isometric and section view of this design. The propulsor is modular and is comprised of 5 aerodynamic components and 1 electric motor (excluding rotor mount and spinner). The assembled propulsor has a length of 167mm and a maximum diameter (at the intake) of 180mm . Design considerations for each component are discussed below.

4.3.2 Shrouded Rotor

The rotor has 11 blades and is shrouded. The shrouding provides additional support during manufacture, preventing blades deforming during 3D printing. The use of support material is minimised as it adversely affects the surface finish of the blades. This is achieved by minimising the distance between the trailing edge and the build plate (located on a $r-\theta$ plane on the downstream side of the rotor).

Reflective aluminium tape is fixed to the outside of the shroud, and coupled with an IR photo-transistor mounted to the casing, to enable measurement of rotor speed.

Maximum stress is expected at the blade-hub interface (minimum chord) and so a fillet of 0.75mm is added to limit stress concentrations. A finite element analysis (FEA) of the rotor at operating speed is undertaken, verifying the maximum stress location. The rotor is fixed at the motor shaft and a centrifugal force is applied with equivalent rotor speed of 6000 RPM. Additionally, a distributed force of 3.47 N is applied to the blades simulating the thrust generated. This corresponds to 58.6% of the total thrust generated by the propulsor,

as shown by Barry^[20]. 1st order elements are used and the local mesh size at the blade hub is set to $\approx 0.1\text{mm}$. The von Mises yield criteria can be expressed as

$$\sigma_{yld} = \sqrt{3}k_{PLA} \quad (4.6)$$

where $k_{PLA} = 33 \text{ MPa}$ is the shear yield strength of 3D printed PLA, as found by Anderson^[21]. This gives a maximum allowable von Mises stress of $\sigma_{yld} = 57.2 \text{ MPa}$. The FEA results, shown in Fig. 4.3, show the maximum von Mises stress to be $\sigma_{vm} = 10.4 \text{ MPa}$ giving a yield margin of safety of 4.5. Displacement is negligible. Shroud clearance to casing is governed by the tolerances required by 3D printing, to avoid rubbing due to shroud eccentricity. The shroud has a thickness of 1mm and there is a 2mm gap corresponding to 5% of span between the rotating shroud and the stationary casing.

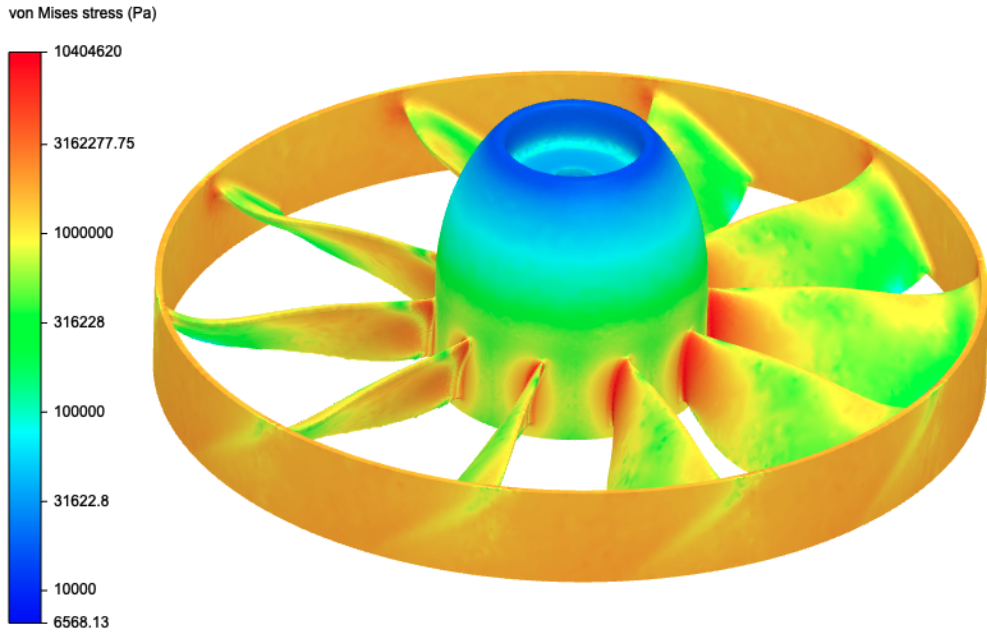


Figure 4.3: Finite element analysis of the rotor at operating speed with colour bar showing von Mises stress on a logarithmic scale

4.3.3 Stator Block: Stator Blades, Casing, and Hub

The 7 stator blades, casing, and hub are one 3D printed part, as shown in Fig. 4.4, with a 75% cubic subdivision infill to maintain rigidity and reduce weight. The blades are both aerodynamic and structural components as the stators transfer the force generated by the fan to the drone chassis, via the casing and arm. The electric motor mounts — with an interference fit to keep rotor centralised — to the mounting plate (see Fig. 4.4). The plate has ventilation holes that match the underside of the motor, allowing airflow to cool the motor

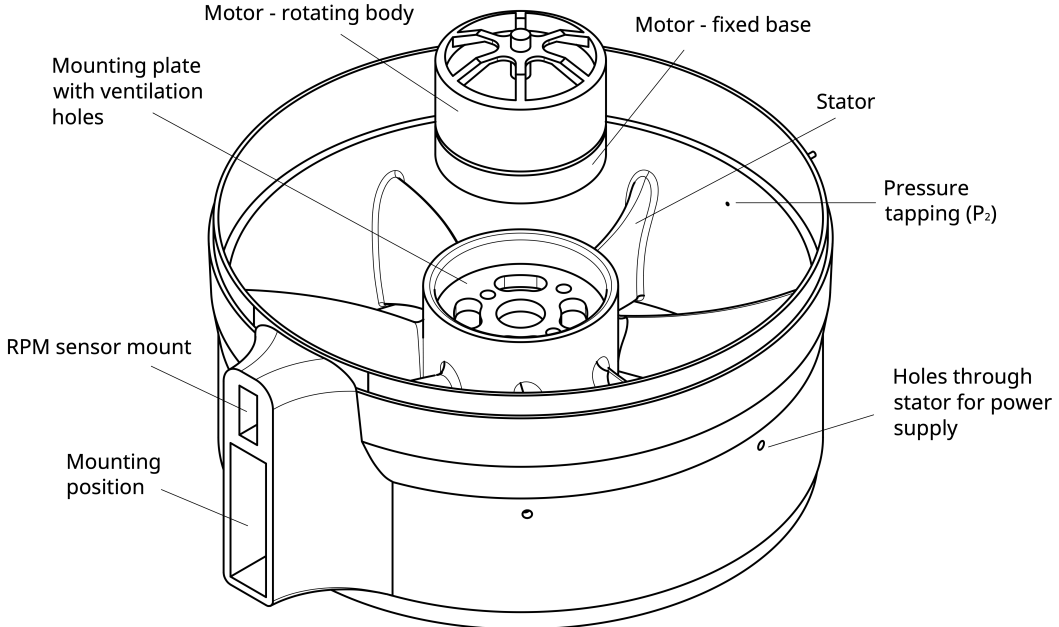


Figure 4.4: Exploded view of stator block and electric motor

and prevent overheating. Although the motor is operating at 20% rated power, maintaining airflow prevents the PLA expanding during operation preventing warping and rubbing.

The ventilation holes allow the 3 power wires on the motor into the hub cavity below the mounting plate, where they are connected to three power supply cables. These power cables are fed from the flying test bed through passages in the stator blades, that can be seen as holes on the casing in Fig. 4.4. The 3D printer generates minimum wall thicknesses of approximately 0.3mm so, to avoid the passage breaking through the stator wall, the passage diameter is less than the maximum stator thickness minus $2 \times 0.3\text{mm}$. At the hub the maximum thickness is 2.15mm therefore the maximum passage width is $2.15 - 2(0.3) = 1.55\text{mm}$. This sets the limit for power supply wire thickness. The same mounting point is used for both stationary tests and hover tests and so the mounting point is sized for an interference fit with the load-cell.

4.3.4 Diffuser

The diffuser is mounted to the stator block with an interference fit. The diffuser casing is also held in place with adhesive tape as it is more prone to detaching under vibration than the hub. Both diffuser hub and casing are designed to be as thin as possible while remaining rigid. At exit the diffuser has a thickness of 1mm and at entry it has a thickness of 2mm .

4.3.5 Intake

The intake is mounted to the stator block with an interference fit. As it generates thrust, it must be securely attached to the stator block and so adhesive tape is also used. The intake is less prone to eccentricity as it has a curved cross-section. It is printed with a constant thickness of 1mm. Print times for the intake can be large (> 1 day) as significant support material is required due to the overhang of the lip.

5 Test Facility Design

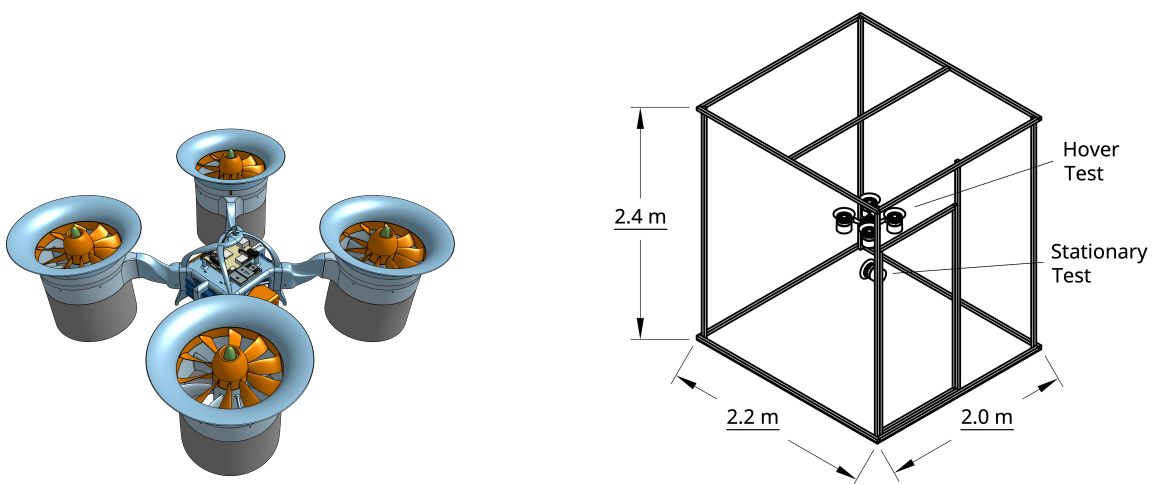
Two types of experiment are undertaken: stationary propulsor tests and hover tests. All testing is done in a purpose built indoor test environment at the Whittle Laboratory, University of Cambridge. Figure 5.1b shows the cage constructed to provide protection from the propulsor and flying test bed. Figure 5.1a shows a render of the flying test bed with ducted fans mounted for hover tests. A retrospective risk assessment analysis is conducted in Appendix B.

5.1 Cage Design & Tether

Figure 5.1b shows the safe indoor test environment constructed for conducting both stationary propulsor and hover tests. The $2.0m \times 2.2m \times 2.5m$ frame is constructed out of $3cm \times 3cm$ section timber beam. An inward opening door provides access to the environment and is hung so that it closes automatically for safety. $1cm$ grid chicken wire walls are fastened securely on each beam. The wire is in tension to increase the frame's rigidity. A central beam crosses the top of the cage and acts as the mounting point for the tether from which the flying test bed is suspended during hover tests. The tether is made from $1m$ of shock cord attached to a long piece of parachute cord using a carabiner. The parachute cord is fed over the central beam on the top of the cage and over the cage edge above the door, allowing the tether to be raised or lowered from outside of the cage.

5.2 System Calibration

System electrical efficiency is estimated by comparing experimentally evaluated figure of merit, $M_{F,exp.}$, for the APC propeller to the manufacturer's calibration data^[8]. The shaft figure of merit, $M_{F,s}$, defined using the power at the motor shaft, $P_s = \Omega \cdot \tau_s$, is determined from the calibration data. Assuming any aerodynamic losses are incurred equally by both experimental and calibration data, the difference in figure of merit can be accounted for by the electrical efficiency of the flying test bed system, η_{sys} .



(a) Perspective render of flying test bed in hover test configuration

(b) Test cage shown in isometric view with flying test bed in hover test configuration and an individual propulsor in the stationary test position (stationary test mount not shown)

Figure 5.1: Test configuration of flying test bed and test environment

$$\eta_{sys.} = \frac{M_{F,exp.}}{M_{F,s}} \quad (5.1)$$

Hereafter this is referred to as the system efficiency.

5.3 Stationary Propulsor Test

Propulsor performance is tested on the stationary test rig, shown in Fig. 5.2, to determine thrust, power, RPM, and motor temperature as well as characterise the aerodynamic performance with static pressure measurements. All electronic connections are made using metallic braid shielded cable. Thrust, power, and RPM data is collected by the flying test bed chassis and the main motor outputs are used to power and control the propulsor. Temperature readings are made using a thermocouple and external thermometer.

5.3.1 Setup

Figure 5.2 shows the experimental setup for stationary tests in the calibration configuration. An aluminium speed-frame structure is fixed to the ground and has a horizontal beam 1m in length mounted 1m high. Thrust, RPM, temperature and pressure measurements require external sensors; their setup is described below. The flying test bed adaptations required for stationary testing are also described.

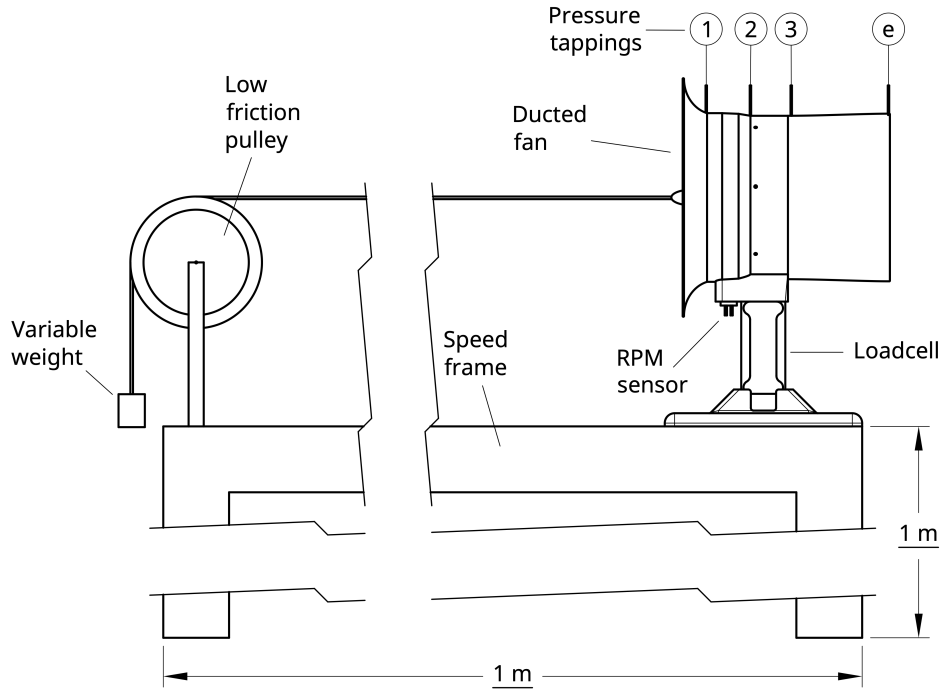


Figure 5.2: Experimental setup of stationary tests in calibration configuration

Load-cell The propulsor is mounted at one end of the frame via a 0.6kg rated single ended shear beam load-cell mounted perpendicular to the axis of the fan. A low friction pulley is mounted to the other end of the frame, with the top of the pulley in line with the axis of the fan. Light-weight high tensile fishing wire, attached to a weight set, is used to apply force to the fan for load-cell calibration. The load-cell connects through an amplifier to the GPIO pins of the RPi3.

IR Photo-transistor The IR photo-transistor inserts with an interference fitted into a slot above the mounting point on the casing, as in Fig. 5.2. A potential divider circuit is connected to the output of the photo-transistor and to the 5V DC/Ground and GPIO pins of the RPi3 via the shielded cable.

Thermocouple The K-type thermocouple is fixed with super glue to the motor mounting plate in the propulsor hub with the sensing junction resting against the base of the motor. The thermocouple is fed through a hollow stator and is plugged into a K-type thermocouple external thermometer from which temperature readings are taken.

Pressure Transducers 1.1mm holes are drilled radially into the casing at 4 axial locations as in Fig. 5.2: p_1 upstream of the rotor; p_2 upstream of the stator; p_3 downstream of the stator; p_e exit from exit duct. 1.1mm outer diameter hypodermic tube tappings are inserted

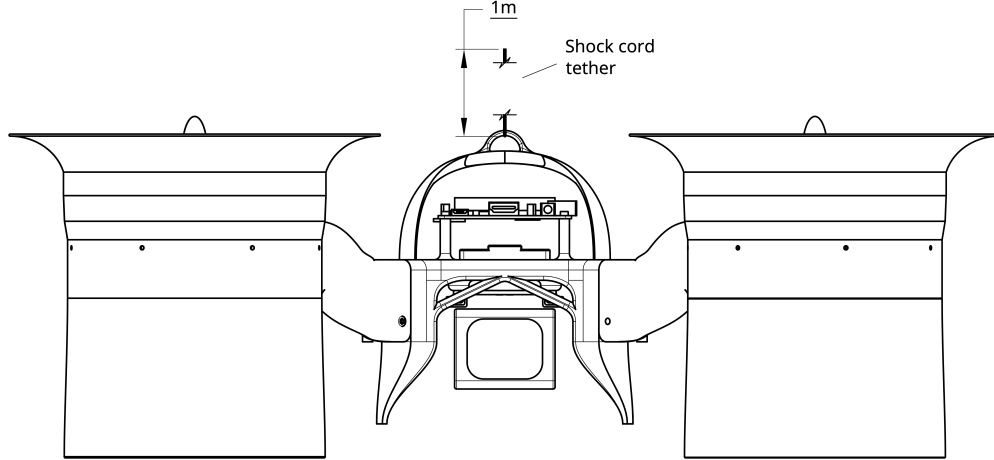


Figure 5.3: Front view of flying test bed in hover configuration

into the holes and secured with super glue on the outside of the casing, ensuring the tapping does not protrude into the flow on the duct side of the casing. Plastic tubing with 1mm inner diameter is fixed to the end of the tappings and connected to input ports of a 16-channel external pressure transducer DSA. The DSA is connected via an ethernet switch to the control station from which gauge pressures (relative to ambient) can be read. The DSA is positioned over 1m away from the propulsor in the $r\text{-}\theta$ plane to reduce the impact of the propulsor on the measured ambient pressure.

5.4 Hover Test

Hover tests are undertaken in the test environment by mounting propulsors to the flying test bed and conducting a static hover from a top-down tether. Figure of merit is determined in-flight by calculating the power required and equating vehicle weight to thrust. Vehicle stability in hover is also considered qualitatively. The propeller results allow the performance in flight to be compared to stationary tests. Further methods of testing are discussed in Section 7.

5.4.1 Setup

The tether ensures the flying test bed is clear of the ground to reduce any ground effect. The tether provides a ‘safety-net’ in the event of a sudden loss in power or emergency situation in which the propulsors must be shutdown. An arched frame is mounted to the flying test bed chassis to attach the tether to the flying test bed and act as a roll cage in the event of a collision with the topside of the chassis, as in Fig. 5.3.

5.4.2 Control

The Pixhawk 4 flight controller attempts to maintain the current altitude and position using its on-board GPS, accelerometers, and gyros. The indoor test environment reduces the GPS accuracy and so manual positional corrections are made using a handheld radio transmitter. Automatic position holding is possible using the forward-right-down ultrasound sensor array.

5.5 Measurement Techniques

Measurements are taken to determine the overall performance in terms of the figure of merit, power, and thrust. Aerodynamic performance is determined in terms of aerodynamic efficiency, pressure coefficients, flow coefficient, and stage loading. All measurements are taken after 5 minutes of continuous system operation to reduce transient temperature effects in the motor and electronics.

5.5.1 Non-dimensional Quantities

Figure of Merit Figure of merit is found using measured or equivalent thrust and required electrical power. Thrust is measured directly using the load-cell in the stationary tests but in the hover tests the thrust is taken as being equal to the flying test bed mass, which is measured prior to flight using a high precision scale. Both load-cell and scales have an accuracy of $\pm 0.1\text{g} \approx \pm 1\text{mN}$. Power is measured as electrical power output from the Pixhawk 4. Readings are accurate but due to noise, particularly during hover tests, they can be imprecise. Taking a mean value over a large window reduces the effect of noise. The flow area is assumed as designed ($A_x = \pi(r_c^2 - r_h^2)$) and air density is calculated from ambient temperature and pressure. Shaft figure of merit is calculated by correcting for the system efficiency $\eta_{sys.}$.

Aerodynamic Efficiency Corrected shaft figure of merit enables an aerodynamic efficiency to be determined as

$$\eta_a = \frac{M_{F,s}}{M_{F,max}} \quad (5.2)$$

where $M_{F,max}$ represents the theoretical maximum figure of merit for a given propulsor. For a propeller $M_{F,max} = 1$ and for a ducted fan with exit duct area ratio σ , $M_{F,max} = \sqrt{2\sigma}$.

Flow Coefficient Flow at inlet is assumed axial and stagnation pressure is assumed equal to atmospheric pressure. Using Bernoulli's equation the axial flow velocity at the casing is determined and the flow coefficient evaluated by dividing by the local blade speed. Taking

the span-wise distribution of flow coefficient to be equal to that determined in Section 3.3.1, the mean-line flow coefficient can be determined.

$$\phi = \phi_m \left(\frac{r}{r_m} \right)^A \implies \phi_m = \phi_c \left(\frac{r_c}{r_m} \right)^{-A} \quad (5.3)$$

$$\therefore \phi_m \approx \left(\frac{V_x}{U} \right)_c \cdot \left(\frac{r_c}{r_m} \right)^{-A} \implies \phi_m \approx \sqrt{\frac{(p_{atm.} - p_1)_c}{\frac{1}{2}\rho(\Omega r_c)^2}} \cdot \left(\frac{r_c}{r_m} \right)^{-A} \quad (5.4)$$

Static pressure p_1 is measured as gauge pressure relative to atmospheric, $p_1 - p_{atm.}$. Rotor RPM is measured using the IR photo-transistor. Casing and mean-line radius are taken as their design values.

Stage Loading Stage loading is estimated by assuming the exit flow from the stator is axial, and due to incompressibility and negligible radial velocity $\partial V_x / \partial x = 0$. Using Bernoulli's equation, the static pressure at stator exit, p_3 , can be related to the change in stagnation pressure as follows

$$\Delta p_0 = p_{03} - p_{01} \implies (p_3 + \frac{1}{2}\rho V_x^2) - p_{01} \xrightarrow{p_{atm.}} \quad (5.5)$$

From Eqn. 3.2 stage loading can be written in terms of Δp_0 and so substituting Eqn. 5.5 gives

$$\psi = \frac{p_3 - p_{atm.}}{\rho U^2} + \frac{1}{2} \left(\frac{V_x}{U} \right)^2 \quad (5.6)$$

where $p_3 - p_{atm.}$ is the measured gauge static pressure. A similar expression to Eqn. 5.4 can be found for stage loading and so the mean-line stage loading can be estimated by

$$\therefore \psi_c = \frac{(p_3 - p_{atm.})_c}{\rho(\Omega r_c)^2} + \frac{1}{2}\phi_c^2 \implies \psi_m \approx \left[\frac{(p_3 - p_{atm.})_c}{\rho(\Omega r_c)^2} + \frac{1}{2}\phi_c^2 \right] \cdot \left(\frac{r_c}{r_m} \right)^{-B} \quad (5.7)$$

Diffuser Static Pressure Recovery Static pressure recovery is written in terms of the measured static pressures as

$$C_{pr} = \frac{p_e - p_3}{\frac{1}{2}\rho V_x^2} = \frac{p_e - p_3}{p_{atm.} - p_1} \quad (5.8)$$

5.5.2 Data Acquisition and Processing

In this section, methods for recording and processing the data streams of thrust, power, RPM, pressure, and temperature are described. Data is collected for ≈ 30 seconds and

mean values are obtained for each data stream. Mean values are used in the analysis and time-sampled data is verified to be steady.

Thrust Prior to each test the load-cell is tared to remove any zero error. The load cell is then calibrated. A Python script on the RPi3 records thrust from load-cell measurements (simultaneously with RPM) and data is wirelessly imported to MATLAB via the SCP protocol. Raw values are compared to the fit obtained during calibration to evaluate the thrust at each data point. The mean thrust is determined.

Power Power is measured by recording the output voltage and current from the PM07 power management board. The maximum sample rate is $\approx 1Hz$, limited by the telemetry data transmission protocol, and so ≈ 30 readings are made. Voltage and current data is obtained through the logging feature on QGroundControl: MavLink Inspector, via the telemetry module. The recorded log is automatically imported into MATLAB for processing. Instantaneous samples of current and voltage are multiplied to determine instantaneous power. A mean power is then determined.

RPM At operating speeds the required IR photo-transistor sample rate, to reliably determine RPM, is 16 kHz. The RPi3 is found to have a GPIO sample rate of 30 kHz hence one RPM sensor is used. A Python script on the RPi3 records RPM from the IR photo-transistor (simultaneously with thrust) and data is wirelessly imported to MATLAB via the SCP protocol. RPM is determined by timing how long it takes for consecutive reflective strips on the rotor shroud to be registered. RPM is calculated by averaging the rotation period over 10 rotations. This reduces the error as the sample location on the leading edge of the reflective strip varies.

Pressure Pressure tappings measure static pressure at the casing. Flow quantities such as flow coefficient are determined at the casing and their mean-line values are estimated from the design span-wise distributions. Pressure is measured from the DSA as gauge pressure relative to atmospheric, $p - p_{atm}$. Measurements are made simultaneously with thrust, power, RPM, and temperature measurements to synchronise the data and account for any transient behaviour. Data is recorded directly into MATLAB on the control station. Non-dimensional quantities are calculated as in Section 5.5.1. The mean is calculated over the 100 readings.

Temperature One K-type thermocouple is fixed to the mounting plate of the electric motor in the ducted fan hub. This is connected via a 1m long cable to a thermocouple thermometer. Whilst data is collected the temperature is monitored to ensure it remains below 50°C, well below the PLA glass transition temperature of 60 – 65°C. Temperature readings are made during the stationary tests but cannot be made during hover tests.

6 Results

6.1 Stationary Propulsor Test

Due to disruption caused by the Coronavirus pandemic (see Appendix A), three ducted fans are tested; A, B, and C. Fan D is not tested. The electrical efficiency of the flying test bed system is first determined. Second, the performance of two different intake designs are compared. Third, the figure of merit is used to analyse the relative performance of the three ducted fans compared to the APC propeller. Finally, the mass model is analysed and the superiority condition evaluated.

6.1.1 System and Electrical Efficiency

Figure 6.1 shows the experimental figure of merit for the APC propeller to vary with RPM by less than 4% in the range of interest, and so the system efficiency is assumed constant in this range. The system efficiency is calculated using the mean values from each data-set and is found to be

$$\eta_{sys.} = \frac{0.301}{0.672} = 45\% \quad (6.1)$$

This is used to evaluate the corrected shaft figure of merit of each propulsor.

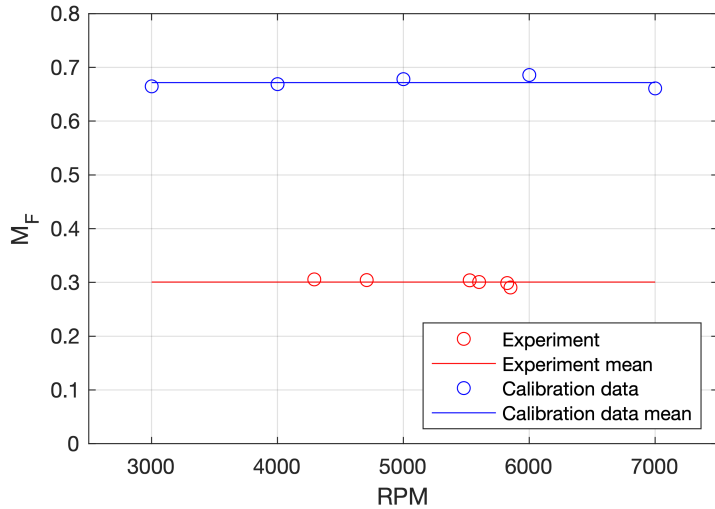


Figure 6.1: Figure of merit for APC propeller from experiment and calibration data

6.1.2 Intake Performance

The two intake designs compared are shown in Fig. 6.2. The short intake produces audibly separated flow, as observed by Hubbard^[22], as the sound pitch and amplitude generated by the fan increased. It is hypothesised that this is due to flow separation at the intake causing either part or full circumference tip stall. No significant variation in tone is observed with the long intake. The figure of merit of the long intake was found to be 30% higher than the short intake thus supporting these observations. The long intake was used in all other tests described here.

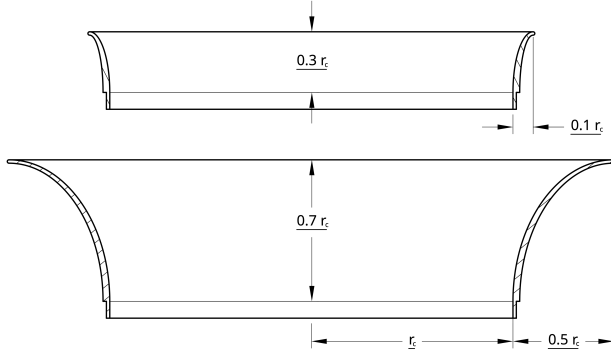


Figure 6.2: Cross-section and dimensions of short and long intake

6.2 Performance Comparison and Discussion

Three prototype ducted fans are tested, with design parameters and results summarised in Table 6.1. Fan A has a constant angle vortex distribution whereas fans B and C are free vortex designs. Fan D is a mixed vortex design but is not tested (see Appendix A). Fan C has a higher quality 3D printer configuration than fan B, but they are otherwise identical. Mean-line flow coefficient and stage loading are evaluated and used to find the equivalent exit duct area ratio, as in Eqn. 3.5. Diffuser static pressure recovery is determined for fans A and B. Experimental and corrected shaft figure of merit are evaluated, and the aerodynamic efficiency determined.

Figure 6.3 shows the ducted fans to have a higher figure of merit than both the propeller in stationary testing, and the theoretical maximum figure of merit for a propeller, $M_{F,max} = 1$. The calculated aerodynamic efficiencies rely on the 3rd party propeller calibration data. The high aerodynamic efficiencies determined may therefore be inaccurate, however their relative magnitudes can still be used to compare propulsor performance. Each fan design shows a steady improvement in performance and this trend was expected to continue to fan D.

The sources of aerodynamic loss, and subsequent variation in figure of merit of the 3 tested fans, are hypothesised to come from 3 main sources. Firstly, profile loss due to flow separation

Fan	Design							Experiment						
	ϕ_m	ψ_m	σ	B	DF _m	N	M _{F,s}	ϕ_m	ψ_m	σ	C _{pr}	M _{F,exp.}	M _{F,s}	η_a
A	0.8	0.25	1.13	-1.1	0.45	7	1.51	0.79	0.29	1.08	0.073	0.52	1.17	0.78
B	0.8	0.25	1.13	-2.0	0.45	7	1.51	0.74	0.33	0.82	0.079	0.58	1.29	0.86
C	0.8	0.25	1.13	-2.0	0.45	7	1.51	-	-	-	-	0.61	1.36	0.90
D	0.8	0.25	1.13	-1.7	0.35	11	1.51	-	-	-	-	-	-	-
Prop.	-	-	-	-	-	2	1.00	-	-	-	-	0.30	0.67	0.67

Table 6.1: Stationary test design parameters and results

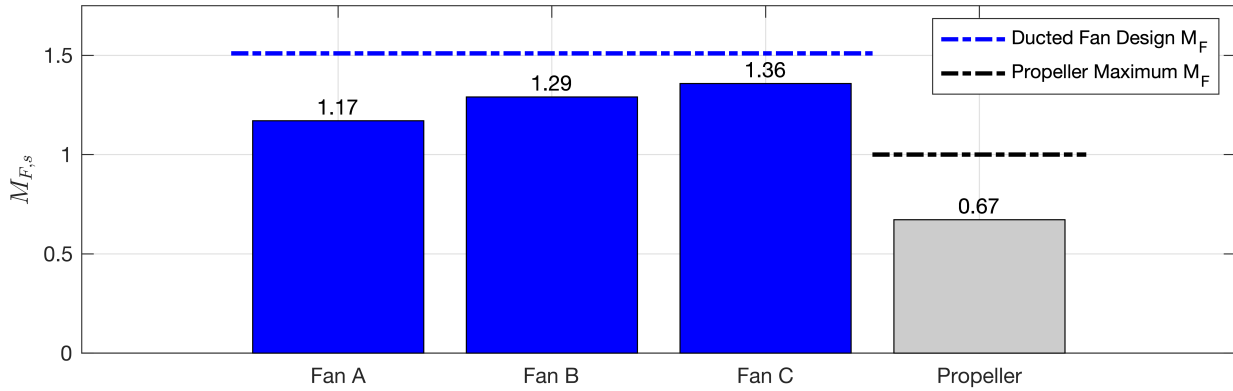


Figure 6.3: Corrected shaft figure of merit for ducted fans compared to propeller data

from the blade — due to low Reynolds number effects — and surface roughness. Secondly, tip loss due to shroud clearance flows and corner separation. Finally, manufacturing techniques introducing geometric deviation from design.

6.2.1 Profile Loss

Fans A and B compare the performance of a constant angle vortex design ($B = -1.1$) and a free vortex design ($B = -2.0$) respectively. Table 6.1 shows the difference in efficiency between the two designs, and resulting difference in figure of merit. Lowering the vortex distribution exponent increases the blade chord at the casing, meaning more momentum is injected into the boundary layer^[23]. This helps the flow remain attached to the casing and results in the experimentally obtained exit area ratio being higher for fan A ($\sigma_{exp.} = 1.08$) than fan B ($\sigma_{exp.} = 0.82$). This moves the operating point of fan B away from design, as shown by experimental ϕ_m and ψ_m in Table 6.1. The Smith chart in Fig. 3.3a shows this operating point to have the same predicted aerodynamic efficiency of $\eta_a \approx 0.94$ and so only a limited increase in profile loss is expected.

Evaluating mean-line flow coefficient allows the variation in Reynolds number across the span to be estimated by assuming the flow coefficient distribution across the span is as

designed. Reynolds number across the span of fan A varies from approximately 10,000 at the hub to 70,000 at the tip whereas fan B varies from 25,000 at the hub to 45,000 at the tip. It is hypothesised that the difference in $M_{F,s}$ between fan A and B is due to the low Reynolds number at the hub of fan A resulting in separation (as shown in Fig. 6.4), due to the Reynolds number being approximately 20% of the Maffioli blade profile design value.

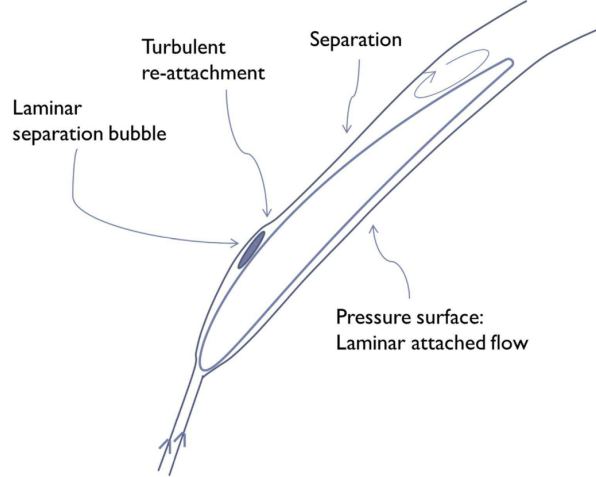


Figure 6.4: Typical boundary layer behaviour for low Reynolds number blade profiles for $Re \approx 50,000$ reproduced from Maffioli *et al.*^[10]

At the tip of fan A, the Reynolds number is above the blade profile design value, meaning the flow remains attached at the trailing edge resulting in minimal profile loss compared to the hub. This results in the flow coefficient and stage loading at the casing being as designed. The evaluated flow coefficient and stage loading at mean-line is therefore within 2% of the design values. This correlation with design is not expected to be achieved at the hub due to separation. The Reynolds number at the hub of fan B is 50% lower than the blade profile design value but the hub chord is $\approx 200\%$ that of fan A and so less separation is expected to have occurred.

The manufacturing process causes span-wise ridges on the surface of the blade as a result of finite thickness 3D printed layers with height $0.1mm \approx 1\%$ of chord. This increases profile loss due to increased skin friction. This roughness could be reduced by printing the blades in a radial direction so that the ridges resulting from printing layers are in the direction of the flow. For this to be possible a 3D printer that uses a cylindrical coordinate system would need to be developed.

6.2.2 Leakage and End Wall Losses

Yoon^[24] describes a loss model due to mixing from shroud clearance flows in compressors. All flow angles are taken in the rotor blade relative frame.

$$\frac{\Theta \Delta s}{\psi U^2} = 2 \frac{\dot{m}_l}{\dot{m}} \left(1 - \frac{\tan \beta_2}{\tan \beta_1} \cdot \sin^2 \beta_1 \right) \quad (6.2)$$

where Θ is temperature and Δs is change in entropy. The ratio of leakage mass flow to mainstream is given by

$$\frac{\dot{m}_l}{\dot{m}} = \frac{g_t}{l} C_D \sqrt{\tan^2 \beta_1 - \tan^2 \beta_2} \quad (6.3)$$

where tip clearance is g_t , blade span is l , discharge coefficient is C_D , and rotor relative inlet and exit flow angles are β_1 and β_2 respectively. Discharge coefficient is not known; a range of $0.5 < C_D < 1$ gives a loss range of $5.5\% < \Delta \eta_a < 11\%$ for the design described in Section 3.3, showing that shroud clearance flows account for over 50% of the loss in fan C, as a result of a shroud clearance of 5% of span. This clearance is required due to 3D printing tolerances. Suggested manufacturing improvements are discussed below. Losses due to corner separation are reduced through the use of lean as in Section 3.3.6.

6.2.3 Diffuser Performance

Diffuser performance is assessed assuming exit flow is straight and parallel. The coefficient of static pressure recovery across the diffusers of fan A and B is presented in Table 6.1. This shows the static-pressure recovery to be considerably lower than designed. Both fan A and B had a pressure tapping upstream (P_3) and downstream ($P_{diff,in}$) of the joining line, where the diffuser casing meets the stator block, at the same design radius. Fan A and B manufacturing issues resulted in the trailing edge of the stator block being rough and slightly eccentric. The static pressure difference should be negligible between $P_{diff,in}$ and P_3 however it is found that for both fan A and B the static pressure loss (normalised by flow velocity) is $(P_{diff,in} - P_3)/0.5\rho V^2 \approx 0.1$. This suggests the flow separated at the joining line resulting in a loss in diffuser performance. The manufacturing issues experienced with fan A and B were resolved for fan C. The increase in efficiency is attributed to improved diffuser performance resulting from improved manufacturing methods.

6.2.4 Manufacturing Process

3D printing the rotor blades introduces geometric deviations from the design in the form of surface roughness, large required clearances (both already discussed) in addition to warping and shrinkage. The FEA conducted in the design section shows the rotor geometry to have negligible deflection under load. However, as high temperatures are required during the 3D printing process, temperature gradients can be expected throughout the structure, imparting thermal strain that can cause warping after cooling. The geometry of the printed part should be analysed using a 3D scanner and any geometric deviation quantified. Potential solutions to

this problem include higher fidelity printing, ambient temperature regulation when printing, controlled cooling after printing, and annealing.

6.2.5 Ducted Fan Mass Model

Figure 6.5 shows the mass model predicted mass compared to the manufactured ducted fan mass. The model predicts the propulsor mass to within 14%, suggesting the mass model is valid at the scale considered here. The model does not consider wiring, the mass of mounting points, or fasteners. These account for the difference between the mass model and the actual mass of the propulsor. It should be noted that mechanical and structural considerations at larger fan diameters and higher thrusts may cause the model to deviate further from the manufactured propulsor, for example a thicker casing will be required at larger fan diameters to maintain structural rigidity. The choice of material and manufacturing method may change with size and application at which point the model may need updating, though the same modelling principles should still be valid.

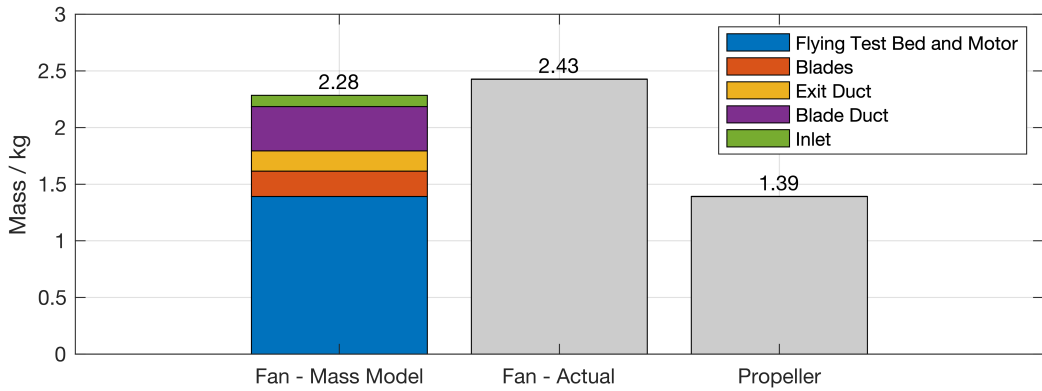


Figure 6.5: Comparison of flying test bed mass when driven by propellers or ducted fans. Mass model is compared to measured mass of vehicle for the ducted fan design

Considering the superiority condition presented in Eqn. 1.13, the LHS of this inequality can now be determined.

$$\frac{W + \Delta W}{W} = \frac{2.43}{1.39} = 1.75 \quad (6.4)$$

This shows that the ducted fan propulsors mounted to the flying test bed accounts for approximately 40% of the vehicle weight. 3D printing ducted fans requires additional material to maintain stiffness. This could be reduced through the use of advanced materials, such as carbon composites, to form a lightweight yet stiff duct and blade structure. Assuming inlet, diffuser, hub and casing thickness can be halved, and taking the density of 61% carbon fibre reinforced plastic (CFRP) as $1600 \text{ kg}\cdot\text{m}^{-3}$ [25], the propulsor weight fraction reduces to

$$\frac{W + \Delta W}{W} = \frac{2.01}{1.39} = 1.45 \quad (6.5)$$

6.3 Superiority Condition

Taking the superiority condition for a non-ideal propeller, Σ is expressed for the general case from Eqn. 1.14 as

$$\Sigma = \left[\frac{(M_{F,s})_{fan}^2 A_{x,fan}}{(M_{F,s})_{prop.}^2 A_{x,prop.}} \right]^{\frac{1}{3}} - \frac{W + \Delta W}{W} \quad (6.6)$$

From experimental data for fan C, Eqn. 6.4, and the determined shaft figure of merit of the propeller, the superiority condition is determined:

$$\Sigma = 0.933 - 1.75 = -0.82 \quad (6.7)$$

The superiority condition is not satisfied, but the superiority parameter Σ agrees with the design value to within 2%. As discussed in Section 3.2.6, the propulsor weight is too large with respect to the payload weight for the superiority condition to be satisfied. In a general application, the propeller area and payload are not fixed and so the superiority condition may be satisfied. The area ratio between the propeller and the fan is given by $\Lambda = A_{x,fan}/A_{x,prop.}$, and the payload weight is W_P .

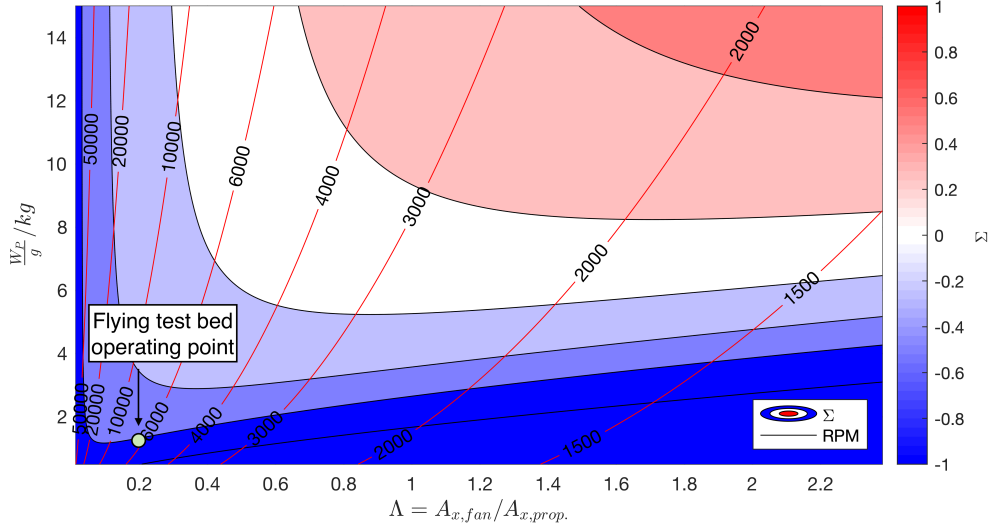


Figure 6.6: Area ratio (Λ) vs. payload (W_P/g) design space showing the superiority parameter given a CFRP construction and experimentally obtained figure of merit. The flying test bed operating point is marked showing $\Sigma < 0$ for all Λ at the flying test bed payload.

Figure 6.6 shows how Σ varies across the Λ -payload design space when a CFRP construction is used and HTR is fixed at 0.2. Figure of merit for the fan and propeller are assumed equal to the experimentally obtained shaft values for fan C and the propeller, 1.36 and 0.67 respectively. Figure 6.6 also shows, provided a minimum area ratio and payload are selected, the superiority condition is satisfied by the ducted fan. For a given payload, it shows there to be an area ratio that maximises the superiority parameter, as contours of Σ have a minima. A Λ design point recommendation can therefore be made given a fixed payload.

6.4 Hover Tests

Hover tests are conducted using the VTOL optimised propeller to verify the agreement with stationary testing. Preliminary results are presented here and compared to those obtained in stationary tests.

6.4.1 Propeller Performance

The figure of merit is recorded as $M_{F,s} = 0.29 \pm 0.05 / \eta_{sys.} \approx 0.65 \pm 0.1$. This suggests that in-flight performance is comparable to stationary test performance.

6.4.2 Hover Test Limitations

The error observed in the flight data was large due to variations in thrust resulting from the control system attempting to maintain position. This resulted in frequent spikes in electrical power. Combining this error with the low sampling rate for power readings made it difficult to determine the exact figure of merit. As the propellers were unshrouded, care was taken to avoid contact with the test cage walls which resulted in significant manual positional corrections. This will improve when testing ducted fans as the casing will provide shielding against contact. As a result of the test environment being small and in close proximity to solid walls, there was significant wall effect further adding to the difficulty to maintain horizontal position. A larger test environment or testing outside on a calm day could be suitable alternatives. More emphasis should be placed on tuning the control system once the ducted fans have been mounted to ensure smooth motion and reduce the magnitude of power spikes.

7 Future Work

This report has acknowledged the open design space for VTOL electric vehicles, and established the validity of pursuing alternative methods of propulsion to the propeller. Further work is needed to better understand the design space, consider other propulsor configurations, and explore the response of a ducted propulsor in a dynamic environment. These ideas are discussed in this section.

7.1 Propulsor Design

7.1.1 Contra-rotating Ducted Fan (CRDF)

The superiority condition adds a design constraint that enables comparative performance to be determined. Consider the superiority condition, as defined in Eqn. 1.14

$$\Sigma = \left[\frac{(M_{F,s}^2 A_x)_{fan}}{(M_{F,s}^2 A_x)_{prop.}} \right]^{\frac{1}{3}} - \frac{W + \Delta W}{W} \quad (7.1)$$

Assuming fixed figure of merit and comparable $A_{x,fan}$ and $A_{x,prop.}$ this suggests the superiority parameter can be increased in two ways. Firstly, the payload could be increased — Fig. 6.6 demonstrates this by evaluating the design at higher payloads. Secondly, thrust density of the propulsor could be increased to reduce the number of propulsors required for hover, thus reducing ΔW . CRDFs replace the stator in a normal ducted fan (NDF) with another rotor spinning in the opposite direction. This means the work done on the flow can double. This increase in work can be ‘cashed-in’ in a number of ways. Assuming each rotor has a flow coefficient and stage loading ϕ_1 , ϕ_2 and ψ_1 , ψ_2 respectively, considering velocity triangles with rotor 1 relative angles β and rotor 2 relative angles γ , and that axial velocity is constant along the duct

$$\frac{\psi_1 U_1}{\tan \beta_2 - \tan \beta_1} = \frac{\psi_2 U_2}{\tan \gamma_2 - \tan \gamma_3} \quad (7.2)$$

It can further be shown that

$$\tan \alpha_1 + (\tan \beta_2 - \tan \beta_1) = (\tan \gamma_2 - \tan \gamma_3) + \tan \alpha_3 \quad (7.3)$$

Hence assuming axial flow at inlet ($\alpha_1 = 0$) and exit ($\alpha_3 = 0$), using Eqn. 7.3, Eqn. 7.2 becomes simply

$$\psi_1 U_1 = \psi_2 U_2 \quad (7.4)$$

Assuming both rotors are loaded equally during steady operation, this suggests they must also have equal rotor speeds. This result is also shown by Waldren *et al.*^[2]. Waldren also

shows that the overall performance of a CRDF stage can be described by considering the pair of rotors in the reference frame of the downstream rotor, such that the machine looks like a NDF with rotor speed $|U_1| + |U_2|$ in a frame of reference rotating at U_2 . The relative frame CRDF non-dimensionals, ϕ' and ψ' , can be related to the absolute frame non-dimensionals, $\phi_{1,2} = \phi$ and $\psi_{1,2} = \psi$, by

$$\psi' = \frac{\phi'^2}{4\sigma^2} \implies \frac{\psi'}{\phi'^2} = 2 \cdot \frac{\psi}{\phi^2} \quad (7.5)$$

As efficiency is governed by the relative frame non-dimensional^[2], this implies that using a CRDF would enable more of the design space to become accessible resulting in higher absolute frame flow coefficients without compromising efficiency. For example, keeping $\psi' = \psi$ implies a higher absolute frame flow coefficient can be achieved whilst keeping the relative frame flow coefficient the same as the NDF design. This gives an absolute frame flow coefficient $\phi = \sqrt{2}\phi'$, resulting in thrust increasing by a factor of 2 meaning half as many propulsors are required and so ΔW decreases. As the relative ducted fan performance is governed only by the figure of merit (a function of exit duct area ratio alone) and flow area (unchanged no matter how many fans are in the passage) the RHS of the inequality will remain unchanged². For example, a design with area ratio $\Lambda = 1$ and payload $W_P/g = 5\text{kg}$ has $\Sigma_{NDF} = -0.03$, but with a CRDF this becomes $\Sigma_{CRDF} = +0.29$ ³.

7.1.2 Computational Fluid Dynamics (CFD)

Empirical results, such as Carter's rule and Lieblein's diffusion factor, are obtained from experiments on compressor cascades, assumed to approximate an infinite radius compressor with a finite span. This assumes secondary flow effects are minimal. However, for a low HTR design at a finite and small radius, the validity of these correlations is unknown. Loss mechanisms and flow behaviour assumptions could be validated using CFD. McEveley^[26] explores the use of CFD in ducted fans and demonstrates corroboration with experiment.

7.2 Stationary Propulsor Experiments

The design discussed for fan D in Section 3 must now be tested. It should be manufactured using the higher quality 3D printing settings used for fan C as this showed a significant improvement in diffuser performance and overall figure of merit. A fan characteristic can be obtained by running the fan with varying back pressure to change the operating point. Ideally an exit traverse would also be undertaken to determine stagnation pressures across the

²Evidence suggests small increases in efficiency may be achieved by using a CRDF^[2] and so the actual figure of merit may increase.

³Evaluated using the mass model described in the design section, with the number of propulsors halved.

annulus and further analyse potential sources of loss. Alternative manufacturing techniques should be considered to satisfy the superiority condition using lighter propulsors. Finally, a comparable CRDF design should be tested to verify increased thrust and constant figure of merit for a lower propulsor weight

7.3 Flying Test Bed Experiments

Two developments are considered here to extend the capabilities of the flying test bed. Firstly, the addition of various sensors to the flying test bed for static hover tests is discussed. Secondly, using the flying test bed to analyse the stability of ducted fans whilst manoeuvring is considered.

7.3.1 Static Hover Test Adaptations

The hover test setup provides multiple interfaces for further data collection through the RPi3. RPM, noise output, and pressures could be added to the flying test bed hover test. Potential setups for these are discussed.

RPM A single RPM sensor can be used during hover tests to ensure the RPi3 sample rate on the IR photo-transistor output is high enough, as is Section 5 to register both reflective strips every revolution, only one sensor can be used. For static hover testing this is sufficient, as each motor should have approximately equal speeds.

Noise Acoustic noise generated by the flying test bed can be measured by an external microphone kept at a fixed horizontal distance, 1m for example. This allows the noise output by the ducted fan and the propellers to be compared.

Optional Pressure Transducers The ADCPi ADC breakout on the RPi3 allows pressure transducers to be connected directly to the flying test bed. Two breakout boards can be stacked to give a total of ($6 + 8 = 14$) pressure transducer inputs (2 inputs from the first ADC are used by the horizontal proximity ultrasounds and each ADC has 8 input channels).

7.3.2 Manoeuvre Tests

One drawback of the ducted design is the presence of the intake and casing upstream of the rotor. In a crosswind, or during horizontal translation of the propulsor, the flow moves across the intake and is at risk of separating off the leading edge of the intake. This results in turbulent flow passing into the windward side of the rotor resulting in a destabilising moment on the propulsor. This moment has been measured in a static wind-tunnel environment^[1]

but the impact on in-flight manoeuvrability is also important. Consider a horizontal manoeuvre in which the flying test bed attempts to achieve a constant horizontal velocity whilst maintaining altitude. The resulting crosswind may begin to separate off the leading lip of the intake, resulting in a decrease in propulsor thrust at the current motor speed. As the propulsor must be angled to provide both forward thrust and lift, a drop in thrust results in a decrease in lift as well as a destabilising moment as in Fig. 7.1. Therefore, the control system would demand a higher motor RPM to ensure sufficient lift. One proposed measure of manoeuvre stability is the power requirement to maintain steady horizontal translation at a fixed altitude, normalised by the power required for static hover.

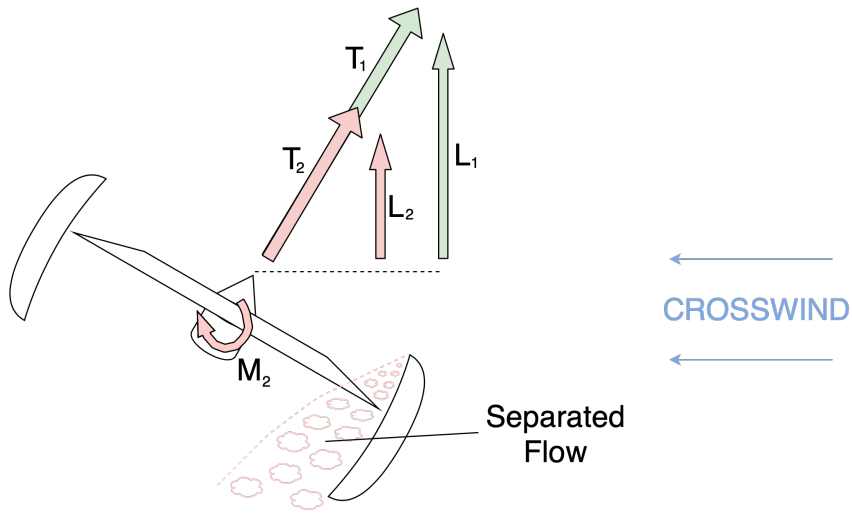


Figure 7.1: Effect of separation of leading lip during horizontal manoeuvre

8 Conclusions

A vehicle with a ducted fan propulsor can consume less power to maintain hover than a propeller — indicated by a positive value of the superiority parameter — provided the application payload relative to propulsor weight is large enough, and the ratio of ducted fan to propeller flow area is large enough.

Specifically, the three research questions proposed in Section 1.3 can now be answered:

- A ducted fan is developed with a design figure of merit of 1.51, achieving $M_{F,s} = 1.36$ in experiment. Aerodynamic efficiency is found to be $\eta_a = 90\%$. Separation, skin friction and shroud clearance flow losses are hypothesised to be the primary sources

of loss. Skin friction and shroud clearance flows can be improved using alternative manufacturing methods.

- The ducted fan does not satisfy the superiority condition when applied to the flying test bed, as the payload is too small. The superiority parameter is predicted within 2% of the experimental value. Suitable ranges of operation in which the superiority condition is satisfied are identified using the mass model (including for fan-propeller area ratios less than 1) by increasing payload and using CRDFs to reduce the number of propulsors required to achieve static hover. CRDFs are identified as the most promising future work opportunity.
- In-flight hover figure of merit is recorded as $M_{F,s} = 0.65$ which agrees with stationary testing in which the figure of merit is evaluated as $M_{F,s} = 0.67$ from manufacturer's calibration data. In-flight data experienced significant noise compared to stationary testing due to the control system attempting to maintain position.

References

- [1] J. L. Pereira, "Hover and wind-tunnel testing of shrouded rotors for improved micro air vehicle design", MARYLAND UNIV COLLEGE PARK DEPT OF AEROSPACE ENGINEERING, Tech. Rep., 2008.
- [2] J. Waldren, C. Clark, S. Grimshaw, and G. Pullan, "Non-dimensional parameters for comparing conventional and counter-rotating turbomachines", in *Turbo Expo: Power for Land, Sea, and Air*, American Society of Mechanical Engineers, vol. 58561, 2019, V02BT40A026.
- [3] A. T. Institute. (2019). Accelerating ambition technology strategy 2019, [Online]. Available: <https://www.ati.org.uk/media/siybi1mm/ati-tech-strategy.pdf> (visited on 05/20/2020).
- [4] L. Schroth. (2019). The drone market 2019-2024: 5 things you need to know, [Online]. Available: <https://www.droneii.com/the-drone-market-2019-2024-5-things-you-need-to-know> (visited on 01/03/2020).
- [5] R. Thomson. (Jan. 2020). Electrically propelled aircraft developments exceed 200 for the first time, [Online]. Available: <https://www.rolandberger.com/en/Point-of-View/Electric-propulsion-is-finally-on-the-map.html> (visited on 05/20/2020).
- [6] T. Zhang and G. N. Barakos, "Review on ducted fans for compound rotorcraft", *The Aeronautical Journal*, pp. 1-34, 2019.
- [7] A. F. Nemnem, M. Y. Zakaria, and A. M. Elzahaby, "Contra-rotating ducted fan aerothermodynamic design procedure for unmanned applications", in *2018 AIAA Information Systems-AIAA Infotech@ Aerospace*, 2018, p. 0745.
- [8] A. P. Composites. (Dec. 2014). Performance data for 10x4.7sf, [Online]. Available: https://www.apcprop.com/files/PER3_10x47SF.dat (visited on 05/23/2020).

- [9] J. Brandt, R. Deters, G. Ananda, and M. Selig. (Dec. 2014). Uiuc propeller database, [Online]. Available: <http://m-selig.ae.illinois.edu/props/propDB.html> (visited on 05/23/2020).
- [10] A. Maffioli, C. Hall, and S. Melvin, “Aerodynamics of low reynolds number axial compressor sections”, in *53rd AIAA Aerospace Sciences Meeting*, 2015, p. 1934.
- [11] E. S. D. Unit, “Performance of circular annular diffusers in incompressible flow”, Engineering Sciences Data Unit, Tech. Rep., 1975.
- [12] R. Corralejo and P. Harley, “Smith diagram for low reynolds number axial fan rotors”, in *12 th European Conference on Turbomachinery Fluid dynamics & Thermodynamics*, EUROPEAN TURBOMACHINERY SOCIETY, 2017.
- [13] S. L. Dixon and C. Hall, *Fluid mechanics and thermodynamics of turbomachinery*. Butterworth-Heinemann, 2013.
- [14] S. Lieblein, F. C. Schwenk, and R. L. Broderick, “Diffusion factor for estimating losses and limiting blade loadings in axial-flow-compressor blade elements”, NATIONAL ADVISORY COMMITTEE FOR AERONAUTICS CLEVELAND OH LEWIS FLIGHT . . ., Tech. Rep., 1953.
- [15] N. Atkins and T. Hynes, *Cued engineering tripos 4a3 turbomachinery i lecture notes, applications and characteristics of turbomachinery*', Oct. 2019.
- [16] A. R. Howell, “Fluid dynamics of axial compressors”, *Proceedings of the Institution of Mechanical Engineers*, vol. 153, no. 1, pp. 441–452, 1945.
- [17] A. Howell, “Design of axial compressors”, *Proceedings of the Institution of Mechanical Engineers*, vol. 153, no. 1, pp. 452–462, 1945.
- [18] A. D. Carter, *The low speed performance of related aerofoils in cascades*. HM Stationery Office, 1950, vol. 29.
- [19] J. V. Taylor and R. J. Miller, “Competing Three-Dimensional Mechanisms in Compressor Flows”, *Journal of Turbomachinery*, vol. 139, no. 2, Oct. 2016, 021009, ISSN: 0889-504X. DOI: 10.1115/1.4034685. eprint: https://asmedigitalcollection.asme.org/turbomachinery/article-pdf/139/2/021009/6305774/turbo\139_02_021009.pdf. [Online]. Available: <https://doi.org/10.1115/1.4034685>.
- [20] J. Barry, “4th year project report: Propulsion systems for vtol electric vehicles”, Cambridge University Engineering Department, Tech. Rep., Jun. 2019.
- [21] I. Anderson, “Mechanical properties of specimens 3d printed with virgin and recycled poly-lactic acid”, *3D Printing and Additive Manufacturing*, vol. 4, no. 2, pp. 110–115, 2017.
- [22] H. H. Hubbard, “Sound measurements for five shrouded propellers at static conditions”, 1950.
- [23] J. Qing, Y. Hu, Y. Wang, Z. Liu, X. Fu, and W. Liu, “Kriging assisted integrated rotor-duct optimization for ducted fan in hover”, in *AIAA Scitech 2019 Forum*, 2019.
- [24] S. Yoon, R. Selmeier, P. Cargill, and P. Wood, “Effect of the stator hub configuration and stage design parameters on aerodynamic loss in axial compressors”, *Journal of Turbomachinery*, vol. 137, no. 9, 2015.

- [25] OnShape. (2020). Onshape materials library, [Online]. Available: cad.onshape.com (visited on 05/23/2020).
- [26] M. McEveley, “4th year project report: Propulsion systems for vtol electric vehicles”, Cambridge University Engineering Department, Tech. Rep., Jun. 2020.

Appendix A: COVID-19

The Coronavirus pandemic resulted in the closure of all University buildings and laboratories on the 22nd of March 2020, as well as an extended period of self-isolation due to illness. This reduced the testing window by 10 weeks.

Tests to Complete

Testing of fan D and complete pressure measurements of fan C were not possible and so fan A, B and C (excluding flow coefficient and stage loading measurements) were used to explore ducted fan performance, and so complete stationary tests of fan C and D should be undertaken. Only hover tests with the APC propeller were carried out, and so hover tests with ducted fans should also be conducted.

Adaptations to Final Report

The report focuses on the design process and presents what data is available to back up the design philosophy. Differences between the design section and the final design of the fans came as a result of access to the Whittle laboratory ending. Significant work was done to render the flying test bed and both stationary and hover test setups and environments in the absence of an opportunity to photograph them.

Appendix B: Retrospective Risk Assessment Analysis

The risk assessment produced at the beginning of the project was followed and the project proceeded without incident. In addition to risk mitigation procedures discussed in the risk assessment, the flying test bed controls were mounted to the outside of the test environment to ensure the anyone controlling the flying test bed had full and unrestricted view of the vehicle in case of emergency.